# Energy Levels and Dynamics of $Tm^{2+}$ Doped into $AMX_3$ Salts

by

**Sophie Koster**

A THESIS SUBMITTED IN
PARTIAL FULFILLMENT OF THE
REQUIREMENTS FOR THE DEGREE OF
MASTER OF SCIENCE
IN PHYSICS


Supervisors: Professor Mike Reid, Associate Professor Jon-Paul Wells
Assistant Supervisor: Professor Roger Reeves
University of Canterbury
2014

# Abstract

Divalent thulium has been doped into $CsCaI_3$, $CsCaBr_3$, $CsCaCl_3$ and $RbCaI_3$ - a series of $AMX_3$ salts. Using previously published optical spectra, a series of parameterised energy level calculations have been performed. The calculated energy levels, optimised crystal field parameters and simulated optical absorption spectra are presented. Theoretical predictions yield excellent approximation to the experimental data.

Temperature dependent fluorescent lifetimes from the ($^3F_4$,$t_{2g}$) and ($^3H_6$,$t_{2g}$) excited (emitting) states have been measured using a pulsed dye laser. For $CsCaBr_3$ and $RbCaI_3$ doped with $Tm^{2+}$, visible emission for the ($^3F_4$,$t_{2g}$) state yields 10 K and 28 K lifetimes of 1.7 $\mu s$ and 0.40 $\mu s$ respectively. In both cases no emission is observed at room temperature. Considering direct multiphonon relaxation to the lower lying ($^3H_6$,$t_{2g}$) levels, a simple energy gap law well accounts for the measured data with effective phonon energies in the range 100-200 $cm^{-1}$ - consistent with the phonon density of states in these low phonon energy hosts. Monitoring infrared emission from the ($^3H_6$,$t_{2g}$) states, 14 K and 10 K lifetimes of 301 $\mu s$ and 250 $\mu s$ are found for $CsCaBr_3$ and $CsCaCl_3$ respectively. For $CsCaBr_3$ this value reduces to 270 $\mu s$ at 200 K and is not quenched until 300 K, whilst for $CsCaCl_3$ emission is quenched by 170 K. This temperature dependent behavior is interpreted in terms of internal conversion via configurational crossing between the excited and ground state potential energy surfaces. Fitting the fluorescence lifetime data to a modified Mott equation, it is inferred that the potential barrier for non-radiative relaxation is five times larger in $CsCaBr_3$ compared to $CsCaCl_3$. This explains the fact that emission is still observable in the bromide host at room temperature.

# Contents

# Figures

# Tables

# Chapter 1

# Introduction

## 1.1 Motivation

Phosphors, or luminescent materials, are used widely in lighting, display, and imaging applications [2]. Lanthanide ions play a crucial part in phosphor materials as the ions often efficiently emit visible light. Thulium is a lanthanide element with electron configuration $4f^{13}6s^2$, and the divalent form of this atom, the $Tm^{2+}$ ion, has the electron configuration $4f^{13}$ [3]. Far fewer studies have been done of $Tm^{2+}$ than of many other lanthanide ions due to the difficulty in stabilising this ion in an oxide or fluoride environment [4]. Some research has however been done into $Tm^{2+}$ doped $CsCaI_3$, $CsCaBr_3$, $CsCaCl_3$ $RbCaI_3$ [1, 2, 4, 5].

While aspects of the spectroscopy of $Tm^{2+}$ are understood, the dynamics of these systems are not fully understood. Performing calculations [6] and fitting the output simulated spectra to the data will allow parameters to be determined and give quantitative physical insight into processes occurring within the ion. Analysing the lifetime of different emissions in these materials will also give more information about these materials. Employing models to fit to lifetime data as a function of temperature allow more output parameters, to give more quantitative information about the different materials.

In $Tm^{2+}$ an upconversion process has been observed, giving visible emission from near infra-red excitation, making this a particularly interesting ion to study. Phosphors are an essential part of creating energy efficient fluorescent lighting, and so this investigation of new materials which can efficiently emit visible light is important and can lead to clues to new technologies.

## 1.2 Thesis Outline

Chapter 2 outlines and explains the underlying physics to this research. The energy level calculations to be undertaken are explained, including the form of the Hamiltonians used and the simulation of absorption spectra from these. The nature of fluorescence lifetimes is then explored. Two methods of modelling the lifetime as a function of temperature are explained: a direct multiphonon relaxation model, and a model of non-radiative relaxation via configurational crossing.

Chapter 3 provides an overview of previous understanding of the divalent thulium and the host materials in which it is to be studied. First the host materials and the integration of $Tm^{2+}$ into them is discussed. Then previous research of emission and absorption processes in $Tm^{2+}$ is presented. Upconversion processes are then explained, including details of those processes observed in $Tm^{2+}$.

Chapter 4 gives a description of the experimental method. First by detailing the synthesis of the materials being used, then by outlining the procedure for measuring the decay of emission from the samples, including a detailed description of the experimental setup and equipment used.

Chapter 5 presents the results from the parametric energy level calculations used to simulate processes within $CsCaCl_3$:$Tm^{2+}$, $CsCaBr_3$:$Tm^{2+}$ and $CsCaI_3$:$Tm^{2+}$. The energy structure of the $Tm^{2+}$ ion is briefly explained, along with the process of performing the calculation. The simulated absorption spectra are then compared to experimental spectra, and the parameters used to achieve the fit are presented and discussed. The energies of the first 55 energy levels are calculated and presented, along with their isotropic dipole strengths, and these are used to identify absorption bands in the experimental spectrum.

Chapter 6 presents the results of fitting two different models to lifetime data as a function of temperature. First a multiphonon model, considering the competition between radiative emission and a cascade of phonons as depopulation methods from a state is considered. Secondly a model considering phonon assisted barrier hopping and radiative emission as competing depopulation methods is considered. For both of these models the fits to the data are presented along with the output parameters. The final part of this

chapter discusses radiative lifetimes calculated as a result of the procedure in chapter 5. These calculated lifetimes are compared to those ouput from the multiphonon model.

Chapter 7 presents conclusions drawn about the results obtained in chapters 5 and 6, providing an overview of analysis undergone in this thesis.

# Chapter 2

# Theory

## 2.1 Energy Level Calculations

Parametric modelling has been succesfully employed to describe the energy levels of many lanthanide systems [3, 7]. To calculate energy levels, Hamiltonians are constructed for different configurations, taking into account many physical parameters, and the energy levels within the states are output as the eigenvalues of the Hamiltonian. In this investigation the states of interest are $4f^N$ and $4f^{N-1}5d$, so the Hamiltonians for these states are explained. The energy levels calculated here can then be used to simulate absorption spectra, which can be fit to experimental data to determine physical parameters.

### 2.1.1 $4f^n$ Hamiltonian

The Hamiltonian of the $4f^n$ levels is given by equation 2.1 [8]. It consists of various parameters which determine the positions of the energy levels.

$$H = E_{avg} + \sum_{k=2,4,6} F^k f_k + \varsigma_f A_{so} + \alpha L(L+1) + \beta G(G_2) + \gamma G(R_7) + \sum_{i=2,3,4,6,7,8} T^i t_i + \sum_{h=0,2,4} M^h m_h + \sum_{k=2,4,6} P^k p_k + \sum_{k,q} B^k_q C^{(k)}_q \quad (2.1)$$

The first term, $E_{avg}$ is an offset which serves the purpose of allowing the ground state energy to be set to zero.

The next term parametrises the Coulomb interaction between the 4f electrons with the radial electrostatic integrals $F^k$ which multiply the angular part of the electrostatic in-

teraction.

The spin orbit coupling constant, $\varsigma_f$, represents the energy shift due to the electromagnetic interaction between the electrons spin and the magnetic field generated by the electrons orbit around the nucleus. It multiplies the angular part of the spin orbit interaction $A_{so}$.

Two electron Coulomb correlation contributions are accounted for with the terms $\alpha L(L+1)$, $\beta G(G_2)$ and $\gamma G(R_7)$. Three electron correlation contributions are accounted for by the term $T^i t_i$ [6].

Magnetically correlated interactions are accounted for by $M^h m_h$, and electrostatically correlated spin-orbit contributions are given by $P^k p_k$ [6].

All of the parameters so far mentioned are called free ion parameters because they have the same form in a free ion as they do in a crystal environment. The terms that represent the non-spherical interaction with the crystal are modelled using the crystal field Hamiltonian, which is the final term in equation **??**. Crystal field splitting involves breaking degeneracies of the electronic levels due to the electrostatic field produced by the negative charges of the surrounding anions, and is described in more detail in section 2.1.3.

### 2.1.2 $4f^{n-1}5d$ Hamiltonian

The $4f^{n-1}5d$ Hamiltonian is the same as the $4f^n$ Hamiltonian for the $4f^{n-1}$ 'core' electrons, and the parameter values are expected to be similar. Additional terms arise due to the 5d electron, and these are shown in equation 2.2

$$H_d = \Delta_E(fd) + \sum_{k=2,4} F^k(fd) f_k(fd) + \sum_{j=1,3,5} G^j(fd) g_j(fd) + \varsigma(dd) A_{so}(d) + \sum_{k=2,4} B^k_q(d) C^{(k)}_q(d) \quad (2.2)$$

The first term $\Delta_E(fd)$ is the energy difference between the $4f^n$ and $4f^{n-1}5d$ levels. The

$F^k$ and $G^j$ account for the Coulomb interaction of the 5d electron with the $4f^{n-1}$ core. $\varsigma(dd)A_{so}(d)$ is the spin-orbit interaction of the 5d electron, and the final term represents d-electron crystal field effects [6].

### 2.1.3 The Crystal Field

Crystal field theory is a model that describes the breaking of degeneracies of electronic orbital states. A free ion has spherical symmetry, with degenerate levels. When an ion is placed in a crystal environment, the spherical symmetry is destroyed, and each level splits under the influence of the electric field produced by the environment [3]. The environment around the ion will usually possess a well-defined symmetry (lower symmetry than spherical.) The degree to which the degeneracy of the states are removed will depend on the point group symmetry in which the ion is located.

The Hamiltonian for a free ion placed in a crystal environment can be written as in equation 2.3 where the total Hamiltonian, $H$, is found by adding the free ion Hamiltonian, $H_F$, to the potential provided by the crystal environment about the ion of interest, $V$.

$$H = H_F + V \tag{2.3}$$

$V$ can be regarded as a perturbation to $H_F$. The potential can be expanded in terms of the tensor operators $C_q^{(k)}$ to give the expression in equation 2.4 [3]. The sum involving $i$ is over all electrons on the ion of interest, and $B_q^{(k)}$ can be considered a coefficient of expansion. This potential is the crystal field part of the Hamiltonian as seen in equations 2.1 and 2.2.

$$V = \sum_{k,q,i} B_q^k(d) C_q^{(k)}(d) \tag{2.4}$$

The specific case of the d orbital in an octahedrally coordinated ion will now be consid-

ered, as this is the case for the $Tm^{2+}$ ions in this study. Figure 2.1 shows the 5d level being split into $t_{2g}$ and $e_g$ states, separated by an energy $\Delta_O$ [9]. This splitting occurs in $Tm^{2+}$, as seen in figure 3.3, with the $t_{2g}$ states being involved in many optical transitions.

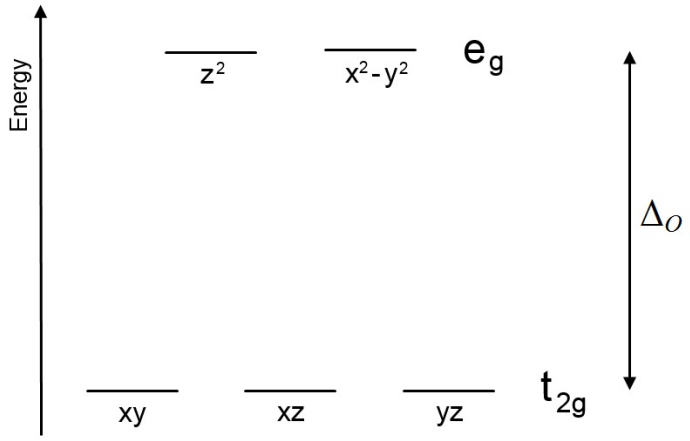


**Figure 2.1** Crystal field splitting of the d orbital of an octahedrally coordinated ion. The 5d state is split into into $t_{2g}$ and $e_g$ states, separated by an energy $\Delta_O$.

The boundary surfaces of the d orbitals in each of these split states is shown in figure 2.2. This is a two dimensional representation and the lobes represent regions of electron density, or regions where it is probable to find the electron. The primary lobes in the $e_g$ states are along the major cubic symmetry axes. Ligands in octahedral symmetry lie along the direction of these axes, meaning there is a strong interaction for these orbitals. The lobes of the $t_{2g}$ states are along directions between the major symmetry axes. There is therefore a weaker interaction for these orbitals. This means that the $e_g$ level is of higher energy than the $t_{2g}$ level [10].

Octahedral symmetry is a relatively high symmetry, and because of this fewer crystal field parameters are required to describe this situation. As the $Tm^{2+}$ ions are approximately octahedrally coordinated, this means that some crystal field parameters can be expressed in terms of others, and not all crystal field parameters are needed in the calculations.

### 2.1.4 Zero Phonon Lines and Vibronic Sidebands

With the positions of the energy levels established, the next step is to consider transitions between these levels. There are two ways electrons can transition between energy

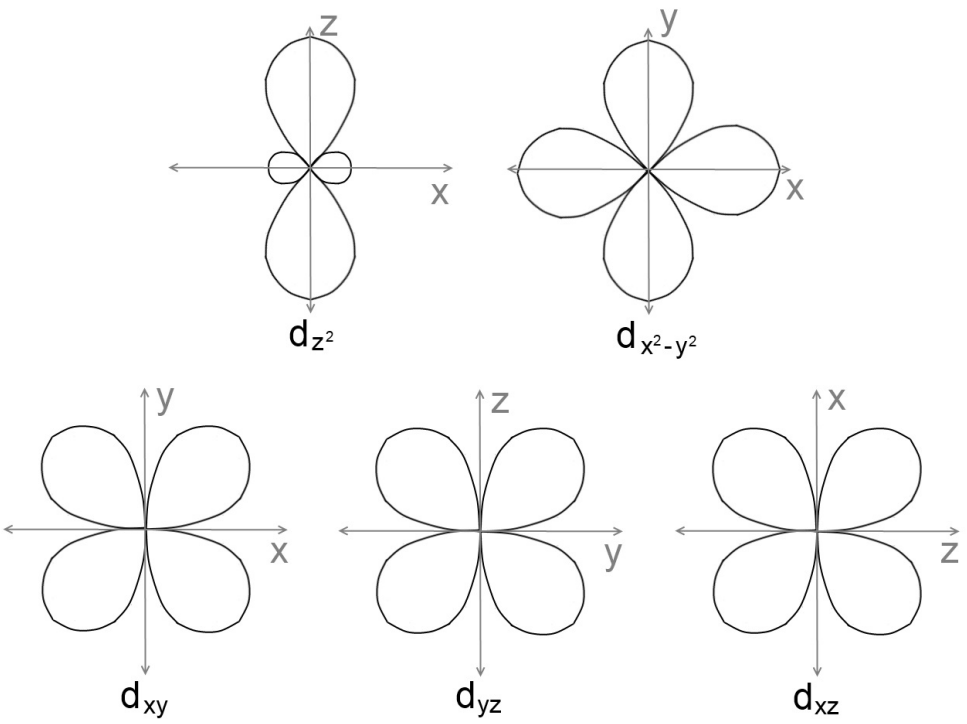


**Figure 2.2** Charge distribution lobes of $t_{2g}$ (bottom) and $e_g$ (top) states. The lobes are shown with respect to the major symmetry axes.

levels, by absorption or emission of photons, quanta of electromagnetic radiation, or by absorption or emission of phonons, quanta of vibrations. Transitions involving photons are called radiative, and transitions involving phonons are called non-radiative. In interpreting absorption and emission spectra the effects of both must be considered to get a realistic physical picture of what is going on.

Figure 2.3 shows two electronic energy levels, a ground and an excited state. The solid horizontal lines represent the phonon energy levels. The horizontal axis is the configurational coordinate, which is proportional to bond length. The zero phonon absorption transition is that from the ground vibrational state of the ground electronic state to the ground vibrational state of the excited electronic state. The energy at which this occurs is the position of the zero phonon band.

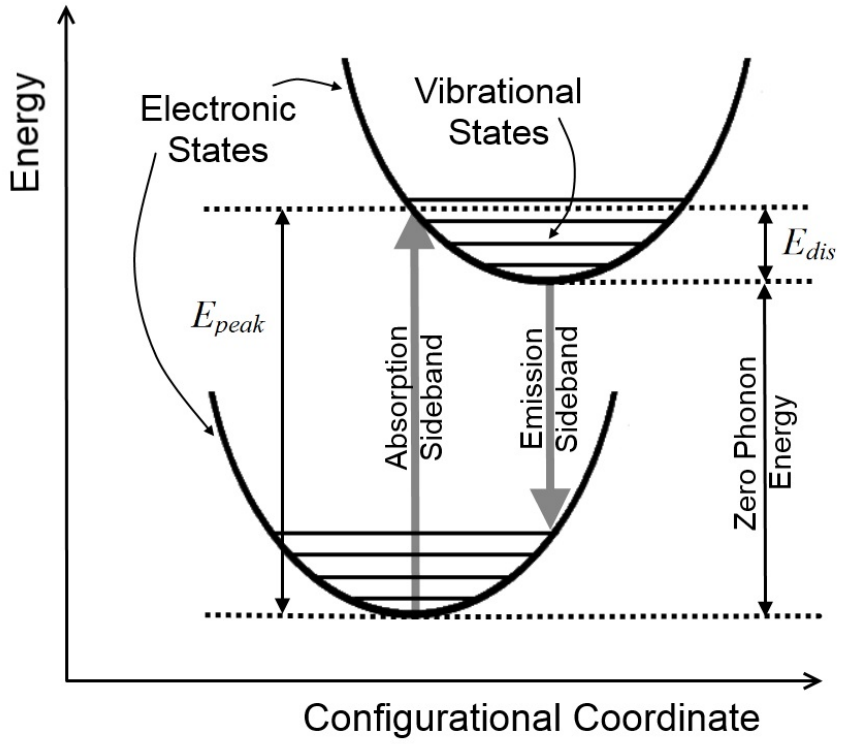


**Figure 2.3** Electronic and vibrational energy levels with zero phonon and vibronic sideband transitions indicated. When electrons are excited to high vibrational levels of the excited electronic excited state, higher energy photons are require than when exciting to the ground vibrational level.

Zero phonon transitions however are not the only type of transitions which can occur. There is vibrational energy in the lattice, and the ions are not always excited to the ground vibrational state of the excited electronic state, they can also be excited into higher energy vibrational states, resulting in higher energy photons being required to excite the electrons into these states, and so a broad absorption band at higher energies than the zero phonon line is observed in absorption spectra. The relative intensities of the zero phonon line and the vibronic sideband are determined by a few factors. Firstly the change in bond length between two configurations plays a role. The bigger the change in bond length, the more likely vibronic transitions are. Large changes in bond length involve the electrons becoming further from the ion and incurring a stronger coupling with the lattice. So transitions involving large changes in bond length have less prominent zero phonon lines. Temperature can also play a role, increasing thermal vibrations in the lattice. It should be noted that the absorption spectra analysed in this report do not have visible zero phonon lines

As can be seen in figure 2.4, in an emission spectrum the vibrational band is on the opposite side of the zero phonon band than in an absorption spectrum. In this situation the availability of higher energy vibrational states decrease the energy of the emitted photons compared to the transition between ground vibrational states from the excited to ground electronic state.

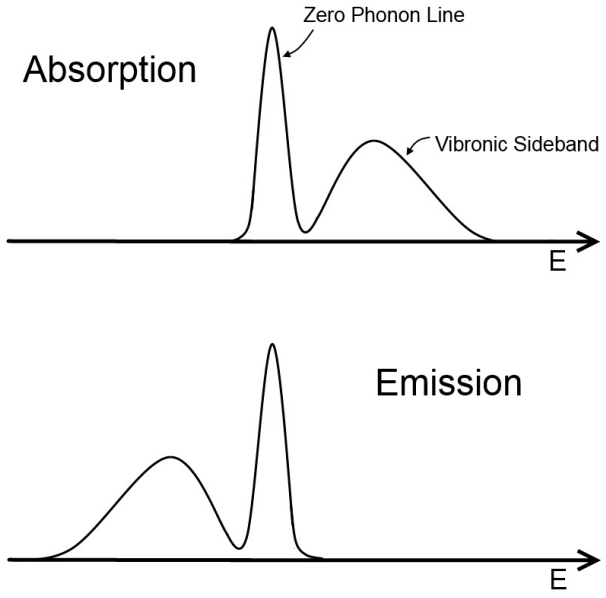


**Figure 2.4** Shape and relative positions of the zero phonon line and vibronic sideband in absorption (top) and emission (bottom) spectra.

The shape of the vibration band is largely dependent upon the electron-lattice coupling in the crystal, or the difference between electron lattice coupling of the ground and excited state. This difference in electron lattice coupling is quantified with the Huang-Rhys parameter given by equation 2.5 [11], where $\omega$ is the vibrational frequency and $E_{dis}$ is defined in figure 2.3.

$$S = \frac{E_{dis}}{\hbar\omega} \tag{2.5}$$

A larger $S$ value corresponds to a larger difference in electron lattice coupling between

the two states. This results in a broader vibrational band, as greater interaction between an excited electron and the lattice (possessing vibrational energy) means more phonon effects present in the transitions between electronic energy levels. This dependence of the absorption band shape upon the Huang-Rhys parameter can be observed in figure 2.5. The vertical lines corresponding to different possible transitions with their lengths proportional to the probability of the transition. The peak of the vibrational band is the energy at which photons are excited from the minimum of the ground state parabola to the intersection of the excited state parabola [12]. This energy is denoted $E_{peak}$ in figure 2.3.

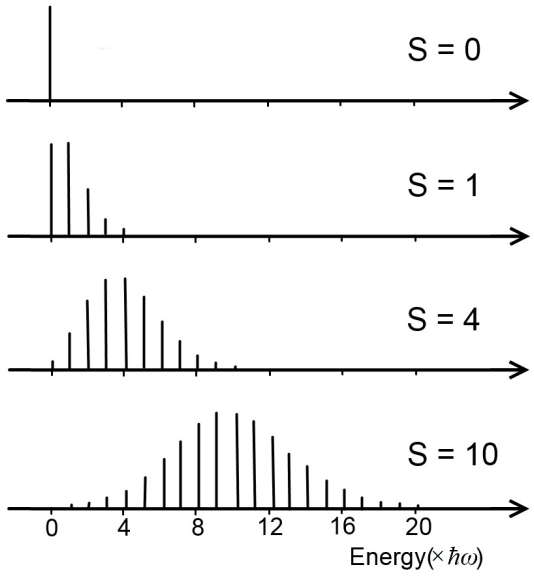


**Figure 2.5** Effect of Huang-Rhys factor, or electron-lattice coupling on shape of spectrum. Greater coupling involves excited electrons interacting more with the surrounding lattice, giving broader vibrational bands

### 2.1.5 Simulating Absorption Spectra

The Hamiltonians of the $4f^n$ and $4f^{n-1}5d$ configurations output the electronic energy levels of these states. The positions of the zero phonon lines can be determined from this as the difference in energy for allowed transitions between $4f^n$ and $4f^{n-1}5d$ states. The intensity of a transition is determined by its oscillator strength, which can be thought of as a transition probability. The absorption oscillator strength is defined in equation 2.6 [6].

$$f_{FI,q}^{ED} = \frac{2m\omega}{he^2}\frac{\chi_L}{n}\frac{1}{g_I}S_{FI,q}^{ED} \tag{2.6}$$

Here $f_{FI,q}^{ED}$ is the oscillator strength, $\omega$ is the frequency of the transition, $h$ is Plancks constant, $n$ is the refractive index, $\chi_L$ is the local correction to the electric field, $g_I$ is the degeneracy of the initial state, and $S_{FI,q}^{ED}$ is the dipole strength for the transition. The dipole strength accounts for the electric dipole moment for the transition between the two states and is shown in equation 2.7. This is the electronic dipole strength for a particular polarisation $q$. $D_q^{(1)}$ is the transition matrix of the electric dipole operator, and sums are over components of the initial and final states.

$$S_{FI,q}^{ED} = \sum_{i,f} e^2 | < Ff | D_q^{(1)} | Ii > |^2 \tag{2.7}$$

Once these positions and strengths are determined, absorption spectra can be simulated by plotting Gaussians or Pekarians offset to the zero phonon lines. Gaussians for high $S$ values, for lower $S$ values a Pekarian curve is needed. The sum of the Gaussians (or Pekarians) from all the zero phonon lines forms a simulated absorption spectra, which can be fit to experimental data to determine physical parameters.

## 2.2 The Thermal Dependence of Fluorescent Lifetimes

When an ion is excited, it remains in an excited state for a time before decaying back to the ground state. When a single ion is considered, the time taken for it to decay is probabilistic. When an ensemble of ions in a lattice are considered, it is possible to determine a mean amount of time for the ion to decay for a given material. This is called the mean lifetime, or just the lifetime. The decay of electrons within an ensemble of ions is an exponential decay, as described by equation 2.8 where $I(t)$ is the intensity of emission at time $t$, $I_0$ is the intensity of emission at time $t = 0$, and $\tau$ is the mean lifetime of the emission. This expression is the Fourier transform of the emitted electric field.

$$I(t) = I(0)\exp(-t/\tau) \tag{2.8}$$

Sometimes multiple decay processes are simultaneously present, and the decay curve observed will then be described by equation 2.9, which is an $N^{th}$ order exponential decay curve.

$$I(t) = \sum_{i=1}^{N} I_i(0)\exp(-t/\tau_i) \tag{2.9}$$

From equations 2.8 and 2.9 the lifetime of a particular emission can be determined by fitting these equations to measured decay data. The lifetime of an emission can be dependent on temperature, so this procedure can be applied to emission data over a variety of temperatures, and a profile of lifetime as a function of temperature can be built up. Two different models for analysing these temperature dependent lifetime profiles will be explored.

### 2.2.1 Direct Multiphonon Relaxation

By considering multiphonon relaxation it is possible to construct a model of the temperature dependence of emission lifetime. To understand this model, the differences between radiative and non-radiative relaxation must first be considered. Radiative relaxation involves an electron in an excited state decaying to a lower energy state by emitting a photon. This process is independent of temperature and the lifetime of this process is characteristic of the material involved. Non-radiative relaxation involves an electron in an excited state decaying to a lower energy state by emitting a phonon. This process is very much dependent on temperature. Increased heat energy in the lattice means more vibrations in the lattice and so more phonon related, non-radiative relaxations. The difference is visually displayed in figure 2.6.

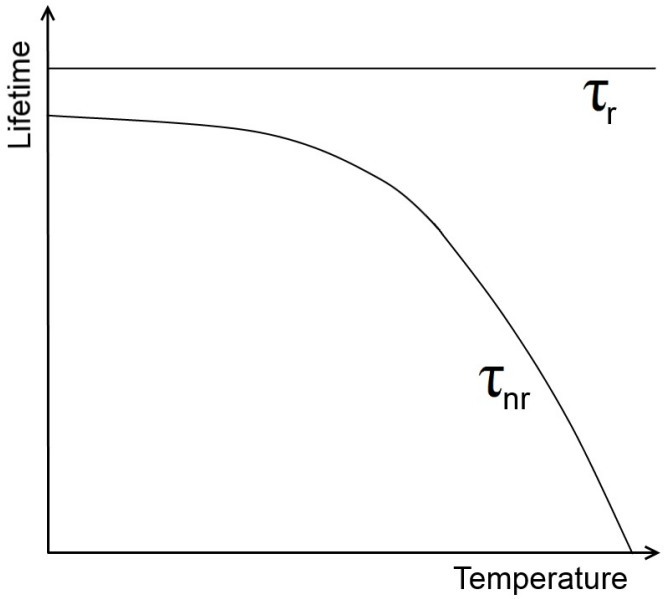


**Figure 2.6** Response of radiative ($\tau_r$) and non-radiative ($\tau_{nr}$) lifetimes to temperature. Increased heat energy in the lattice shortens the non-radiative lifetime, while the radiative lifetime remains unchanged.

The experimentally measured lifetime of a material is a result of the combination of these two factors. At higher temperatures the non-radiative lifetime can be sufficiently long for there to be time for radiative decay to occur. As the temperature increases, the increased phonon presence in the lattice shortens the non-radiative lifetime so that radiative decay becomes less prevalent.

Next the scheme presented in figure 2.7 must be considered. There are three energy levels, a ground state and two excited states. There are two emissions, a higher energy emission $A$ and a lower energy emission $B$.

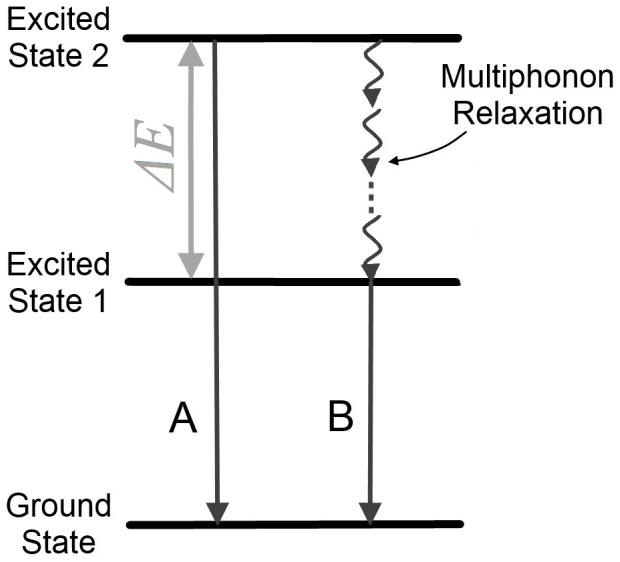


**Figure 2.7** Multiphonon relaxation. Emission $A$ is the result of a simple radiative transition, emission $B$ involves a multiphonon relaxation process followed by a radiative transition from a lower lying state.

The multiphonon relaxation process can be seen to consist of multiple phonons bridging an energy gap $\Delta E$. If the energy of a single phonon is said to be $\hbar\omega$ and there are $N$ phonons required to bridge the gap $\Delta E$, then it can be stated that $\Delta E = N\hbar\omega$.

Emissions $A$ and $B$ are competing processes. Emission $A$ is a simple radiative relaxation from the higher excited state. Emission $B$ is more complicated, involving a multiphonon relaxation process to the lower excited state, followed by a radiative relaxation to the ground state. As the lattice gets warmer the phonon presence in the lattice shortens the purely non-radiative lifetime, making phonon processes more prevalent and causing the emission $B$ to dominate. This means that the ratio of the intensity of emission of $A$ to $B$ can give information as to which process is dominant.

The purpose of investigating this multiphonon process here is to acquire a model with which quantatitive information about $Tm^{2+}$ can be determined. The non-radiative lifetime as a function of temperature is given by equation 2.10 [13, 14]. Here $\tau_{nr}(T)$ is the non-radiative lifetime as a function of temperature, $\tau_{nr}(0)$ is the non-radiative lifetime at 0 K, $\hbar\omega_{eff}$ is the energy of the effective phonon modes involved, $k_B$ is Boltzmann's constant, $T$ is the temperature in Kelvin, and $N$ is the number of phonons needed to bridge the energy gap (or the order of the process.)

$$\tau_{nr}(T) = \tau_{nr}(0)\left[1 - \exp\left(\frac{\hbar\omega_{eff}}{k_B T}\right)\right]^N \tag{2.10}$$

An equation with the total, experimental lifetime ($\tau_{exp}$) as the subject is desired, so the relationship between $\tau_{exp}$, $\tau_{nr}$ and $\tau_r$ is shown in equation 2.11.

$$\frac{1}{\tau_{exp}} = \frac{1}{\tau_{nr}} + \frac{1}{\tau_r} \tag{2.11}$$

Combining equations 2.10 and 2.11 then allow an equation to be formed with $\tau_{exp}$ as the subject. This is presented as equation 2.12.

$$\tau_{exp}(T) = \frac{1}{\left(\tau_{nr}(0)\left[1 - \exp\left(\frac{\hbar\omega_{eff}}{k_B T}\right)\right]^N\right)^{-1} + \frac{1}{\tau_r}} \tag{2.12}$$

This equation can then be used to fit to experimental data. Quantitative results in the form of parameters can be taken from this, allowing information on $Tm^{2+}$ to be gathered. Parameters from different host materials can be compared, and physical conclusions about $Tm^{2+}$ can be drawn.

### 2.2.2 Non-Radiative Relaxation via Configurational Crossing

A second model of temperature dependence of the fluorescence lifetime can be derived by considering potential barriers. A rectangular potential barrier is shown in figure 2.8. This potential barrier has height $V_0$ and width $x$. If an electron has an energy less than $V_0$, then in order to overcome this barrier it must either gain energy (via phonons) to jump over the barrier, or it may tunnel through the barrier. In a real physical system like an ion the barrier is not rectangular, but the same general rules apply for traversing the barrier.

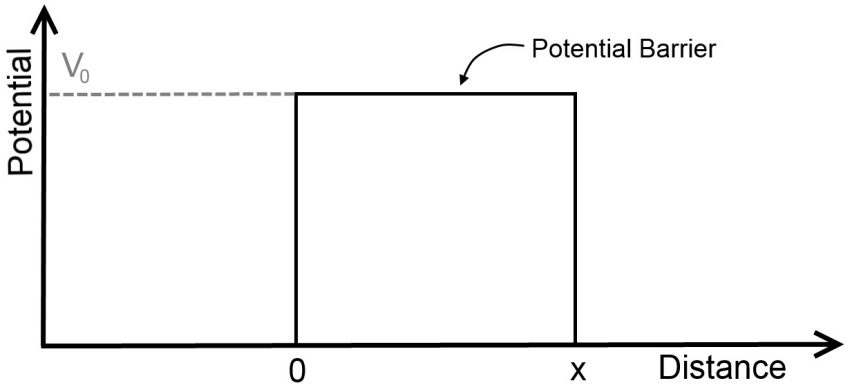


**Figure 2.8** Rectangular potential barrier. For an electron to pass the barrier it must either gain the energy to jump over the barrier or tunnel through it.

When an electron is in an electronic state within an ion, it is in a potential well, as can be seen by the parabolas in the configurational coordinate diagram in figure 2.9. The parabolas represent the potential energy of the states as a function of bond length. Without phonon presence an electron will settle into the energy at the minimum of a parabola, but phonons give the electron extra vibrational energy, allowing it to move along the parabola. When a non-radiative relaxation occurs, an electron needs to gain enough vibrational energy to move up along the parabola of the excited state, to the point where the parabolas cross over, at which point it can relax down along the ground state parabola, releasing phonons of energy to settle into the minimum.

The vibrational energy required for the electron to reach the crossing point between the two parabolas is called the non-radiative energy barrier, and the barrier height is represented by $E_{nr}$, as shown in figure 2.9.

This situation occurs due to the energy levels involved being from different orbitals. This results in a configurational shift seen in figure 2.9. In the case of intraconfigurational transitions, there is no configurational shift between the states, and the parabolas in 2.9 do not intersect, or intersect in such a way that $E_{nr}$ is so large that it can not be overcome, making this sort of relaxation impossible in those cases. Another way to consider this is that when a configurational shift occurs, the electron is displaced further into the lattice, incurring a stronger electron-lattice coupling. This renders the electron more prone to the effects of phonons in the lattice, such that the configurational shift has made the barrier able to be overcome.

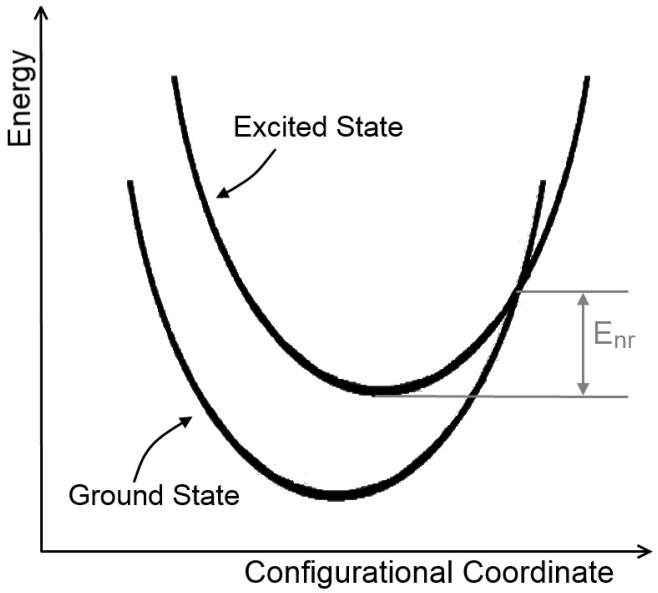


**Figure 2.9** Barrier energy for non-radiative processes. In order for an electron to non-radiatively decay from the excited to ground state, it needs to gain enough vibrational energy to move up along the parabola of the excited state, to the point where the parabolas cross over. This energy is the energy $E_{nr}$.

The purpose of understanding these concepts is to utilise them in building a model of lifetime as a function of temperature. The dependence of the non-radiative lifetime as a function of temperature is shown in equation 2.13 [15, 16]. Here $\tau_{nr}(T)$ is the non-radiative lifetime of emission as a function of temperature, $W_0$ is the rate of non-radiative

depopulation of the zero phonon level of the emitting state (and can be considered the probability of tunneling through the potential barrier,) $W_1$ is the rate of phonon assisted barrier hopping, $E_{nr}$ is the barrier height, $k_B$ is Boltzmanns constant, and $T$ is the temperature in Kelvin.

$$\tau_{nr}(T) = \frac{1}{W_0 + W_1 \exp\left[\frac{-E_{nr}}{k_B T}\right]} \tag{2.13}$$

To get the equation in the form of having $\tau_{exp}$ as the subject, the relationship in equation 2.11 in section 2.2.1 is again implemented to establish the result in equation 2.14.

$$\tau_{exp}(T) = \frac{1}{W_0 + W_1 \exp\left[\frac{-E_{nr}}{k_B T}\right] + \frac{1}{\tau_r}} \tag{2.14}$$

From this equation it can be noted that the constants $W_0$ and $\frac{1}{\tau_r}$ can simply be grouped together, as they cannot be meaningfully discerned in fitting this equation to experimental data. Redefining $W_0 = W_0 + \frac{1}{\tau_r}$ the expression is altered as in equation 2.15.

$$\tau_{exp}(T) = \frac{1}{W_0 + W_1 \exp\left[\frac{-E_{nr}}{k_B T}\right]} \tag{2.15}$$

This equation can then be used to fit to experimental measurements of the lifetime, allowing physical conclusions to be drawn about $Tm^{2+}$ as parameters are compared between different samples.

# Chapter 3

# Background Review

## 3.1 Host Materials

The host materials in which the divalent thulium is studied in this report are a series of $AMX_3$ salts - $CsCaCl_3$, $CsCaBr_3$, $CsCaI_3$ and $RbCaI_3$. Additionally, $Tm^{2+}$ doped into $SrCl_2$ is also studied to a lesser degree. $CsCaCl_3$, $CsCaBr_3$ and $CsCaI_3$ have a perovskite lattice structure, which is shown in figure 3.1. Here the green ions represent the $Cs^+$, the red ions represent the $Ca^{2+}$ and the blue ions represent the $I^-$, $Br^-$ or $Cl^-$ ions. When the $Tm^{2+}$ is doped into the material, it takes the place of some $Ca^{2+}$ ions, at the red sites.

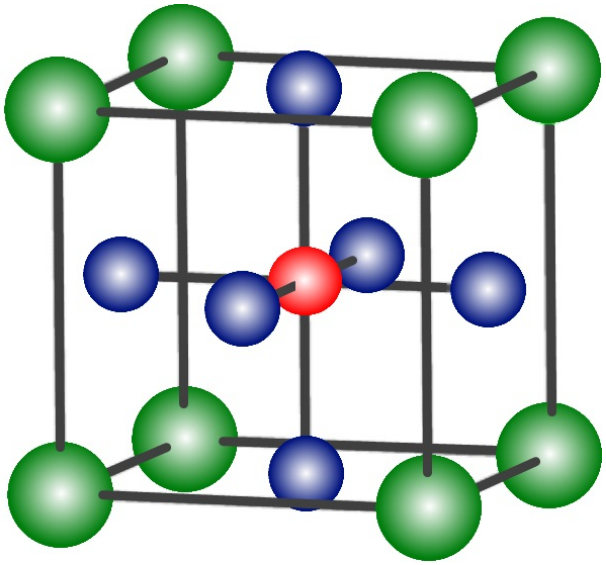

**Figure 3.1** The perovskite lattice structure. Here the green ions represent the $Cs^+$, the red ions represent the $Ca^{2+}$ and the blue ions represent the $I^-$, $Br^-$ or $Cl^-$ ions. When the $Tm^{2+}$ is doped into the material, it takes the place of some $Ca^{2+}$ ions, at the red sites.

The $SrCl_2$ host has a fluorite structure, as shown in figure 3.2. Here the green ions represent the $Sr^{2+}$ and the blue ions represent the $Cl^-$ ions. When the $Tm^{2+}$ is doped into

the material, it takes the place of some $Sr^{2+}$ ions, at the green sites.

$CsCaBr_3$ is a cubic perovskite at room temperature, with space group $Pm\bar{3}m$ and with distorted $O_h$ symmetry on the $Ca^{2+}$ site. The lattice undergoes a phase transition at lower temperatures and crystalises as orthorhombic, with space group $Pnma$ [1].

Like $CsCaBr_3$, $CsCaCl_3$ is a cubic perovskite at room temperature, with space group $Pm\bar{3}m$ and with distorted $O_h$ symmetry on the $Ca^{2+}$ site. This lattice also undergoes a phase transition at lower temperatures and in this case crystalises as tetragonal, with space group $P4/mbm$ [1].

$CsCaI_3$ is also a perovskite, stable in the orthorhombic $Pbnm$ space group at all temperatures [1]. At 10 K this material is isomorphous to $CsCaBr_3$. The $Ca^{2+}$ ion is also octahedrally coordinated with a distortion.

$RbCaI_3$ has a smaller singly charged cation ($Rb^+$) compared to $CsCaI_3$ ($Cs^+$). This leads to a change in structure of the lattice. Here, there is a 'double chain' lattice structure. The lattice is orthorhombic with space group $Pbnm$, and $Ca^{2+}$ ion is octahedrally coordinated like in $CsCaI_3$. The distortion from $O_h$ symmetry is bigger in this case [17, 18].

$SrCl_2$ crystalises in the fluorite structure in space group $Fm3m$. The $Sr^{2+}$ site has $O_h$ symmetry [5].

Equation 3.1 is the dispersion relation for phonons in a one dimensional lattice, which is an expression for the vibrational frequency $\omega$ in a lattice. It is considering an alternating array of two types of ion or atom with masses $m_1$ and $m_2$ repeated periodically at distance $a$ and connected by springs of spring constant $K$. Although this expression describes a one dimensional system, it can be used to draw conclusions about real three dimensional lattices.

$$\omega^2 = K\left(\frac{1}{m_1}+\frac{1}{m_2}\right) \pm K\sqrt{\left(\frac{1}{m_1}+\frac{1}{m_2}\right)^2 - \frac{4\sin^2(ka/2)}{m_1 m_2}} \tag{3.1}$$

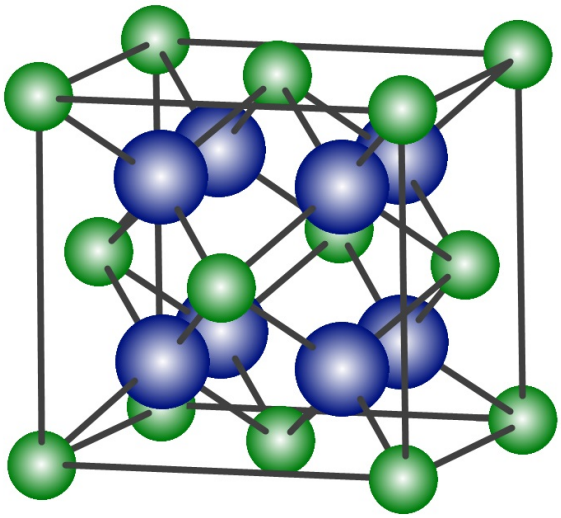

**Figure 3.2** The fluorite lattice structure. Here the green ions represent the $Sr^{2+}$ and the blue ions represent the $Cl^{-}$ ions. When the $Tm^{2+}$ is doped into the material, it takes the place of some $Sr^{2+}$ ions, at the green sites.

From equation 3.1 it can be noted that the vibrational frequency is inversely proportional to the square root of the mass of the ions $\left(\omega \propto \frac{1}{\sqrt{m_1 m_2}}\right)$. It can also be noted that the vibrational frequency is proportional to energy $E \propto \omega$. From these relations it can be concluded that heavier atoms/ions in a lattice result in a lower vibrational energy for the lattice.

The materials being studied are known to have low phonon energies [5]. This can be explained by considering that the anions ($Br^{-}$, $Cl^{-}$, $I^{-}$) involved in these lattices are relatively heavy, which via the reasoning in the preceding paragraph results in lower vibrational energy. This means that fewer non-radiative processes occur, meaning there is less competition for radiative processes and so there are ideal conditions to study radiative processes within the ion.

These materials are very hygroscopic, meaning they absorb water out of the air. For this reason the samples are in an inert atmosphere and sealed within quartz ampoules containing inert atmospheres.

## 3.2 $Tm^{2+}$ Emission

Thulium is a lanthanide element with electron configuration $4f^{13}6s^2$, and the divalent form of this atom, the $Tm^{2+}$ ion, has the electron configuration $4f^{13}$ [3]. Far fewer studies have been done of $Tm^{2+}$ than of many other lanthanide ions due to the difficulty in stabilising this ion in an oxide or fluoride environment [4]. Some research has however been done into $Tm^{2+}$ doped $CsCaI_3$, $CsCaBr_3$, $CsCaCl_3$ and $RbCaI_3$ [1, 2, 4, 5, 19]. These materials are very hygroscopic, and so are held within inert atmospheres in quartz ampoules.

Emission and absorption spectra have been taken of these divalent thulium doped crystals. From examination of the intensities and positions of the transition peaks, insight into the energy level structure of the ion has been achieved [1], along with an understanding of non-radiative relaxation processes [4].

Figure 3.3 is a configurational coordinate diagram showing the energy levels within $Tm^{2+}$ which are relevant to understanding the transitions which have been observed. This model was derived from measurements from $CsCaBr_3$:$Tm^{2+}$ [1], but the general structure has been shown to be true for $CsCaI_3$:$Tm^{2+}$[5], $CsCaCl_3$:$Tm^{2+}$[5], $SrCl_2$:$Tm^{2+}$[19] and $RbCaI_3$:$Tm^{2+}$[18]. The $(4f)^{13}$ and $(4f)^{12}(5d)^1$ configurations can both be seen, with a change in bond length between them being present due to the electron being promoted. This results in the emissions between the configurations being broader than the emission A within the $(4f)^{13}$ configuration. Coulomb repulsion and spin-orbit coupling split the $(4f)^{12}$ configuration into a $Tm^{3+}$ like pattern of terms. The crystal field splitting causes the 5d orbital to be split into $t_{2g}$ and $e_g$, with $t_{2g}$ states being the only relevant states in considering observed emissions. The isotropic exchange part of the 4f-5d repulsion splits the ($^3H_6$,$t_{2g}$) state into high and low spin components [1]. It should be noted that although in figure 3.3 an increase in bond length is shown between the $(4f)^{13}$ and $(4f)^{12}(5d)^1$ states, some studies suggest it may actually be a contraction [20].

The emission A is 4f-4f emission from $^2F_{5/2}$ to $^2F_{7/2}$ states. The emission is very weak up to about 200 K. This is because at low temperatures the higher lying f-d states are metastable and emitting radiatively. Above 200 K the increased thermal energy causes the higher lying states to non-radiatively relax, feeding energy into the $^2F_{5/2}$ state so that

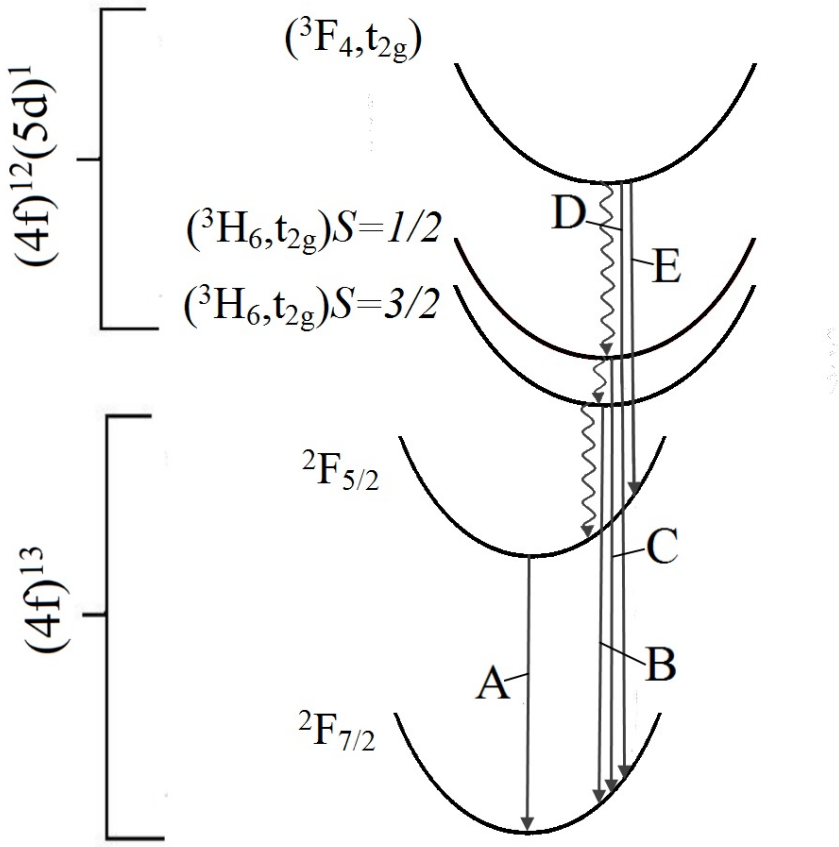


**Figure 3.3** Configurational coordinate diagram of energy levels within $Tm^{2+}$ which are relevant to understanding the transitions which have been observed. Radaitive relaxation is indicated with straight arrows and non-radiative relaxation is indicated with curly arrows.

the A emission can occur [1].

The emission B is a 'spin forbidden' 5d-4f transition from $(^3H_6,t_{2g})S=3/2$ to $^2F_{7/2}$. This emission is weak at low temperatures but at around 100 K it becomes the dominant emission. This is because at around 100 K, the higher $(^3F_4,t_{2g})$ state stops radiating (emission D) and instead it non-radiatively relaxes, feeding energy into $(^3H_6,t_{2g})S=1/2$ which then in turn feeds energy to( $^3H_6,t_{2g})S=3/2$, so that this state now has energy to emit radiatively in the form of the B emission.[1]

The emission C is a 'spin allowed' 5d-4f transition from $(^3H_6,t_{2g})S=1/2$ to $^2F_{7/2}$. The low vibrational energy of the lattice and spin allowed nature of the radiative transition to the ground state mean that the emission C will occur. The photon ratio of emissions C/B is 1/10 at around 10 K and decreases with increasing temperature. This means that the non-radiative depopulation of $(^3H_6,t_{2g})S=1/2$ is dominant at all temperatures [1].

The emission D is a higher excited state 5d-4f transition from $(^3F_4,t_{2g})$ to $^2F_{7/2}$. This emission dominates below 100 K. At low temperatures the $(^3F_4,t_{2g})$ state is metastable and the radiative emission is competitive, but above about 100 K non-radiative relaxation becomes dominant. (This is true of $CsCaBr_3$:$Tm^{2+}$, in $CsCaCl_3$:$Tm^{2+}$ the emission is weaker and rapidly quenched [1].)

The emission E is an inter-excited state 5d-4f transition from $(^3F_4,t_{2g})$ to $^2F_{5/2}$. This transition has the same temperature dependence and originating state as the D emission. The photon ratio of emissions E/d however is only 1/800. This can be attributed to the $\Delta J = 1$ selection rule [10]. The lowest energy state of the $(^3F_4,t_{2g})$ multiplet has dominantly $J = 9/2$ character, thus the transition to $^2F_{7/2}$ is allowed, while the transition to $^2F_{5/2}$ is forbidden [1].

## 3.3 $Tm^{2+}$ Absorption

Absorption spectra have been taken of $CsCaBr_3$:$Tm^{2+}$, $CsCaI_3$:$Tm^{2+}$, $CsCaCl_3$:$Tm^{2+}$ [19], $RbCaI_3$:$Tm^{2+}$ [17, 18], and $SrCl_2$:$Tm^{2+}$ [21]. The measured absorption spectrum [1] is shown in figure 3.4(c) for $CsCaBr_3$:$Tm^{2+}$. For all the samples in this report, the energies of particular features are different, but the general features are similar.

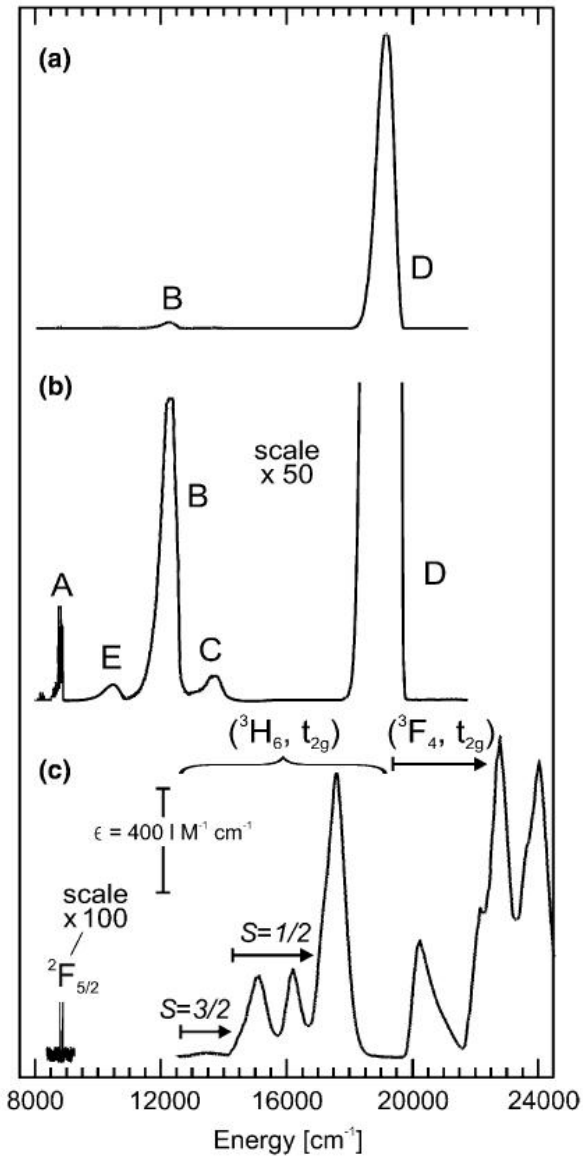


**Figure 3.4** Absorption and emission spectra of $CsCaBr_3$:$Tm^{2+}$ taken at 10K and excited at 21,834 $cm^{-1}$ [1].

Figure 3.4 (a) and (b) are emission spectra, and the five emissions detailed in section 3.2 can be seen here. There are both 4f-4f and 4f-5d features present.

The 4f-4f features in the absorption spectrum are the lowest energy, sharp lines seen at around 8800 $cm^{-1}$ [4]. They are sharp because they are due to transitions occurring between the $^2F_{7/2}$ and $^2F_{5/2}$ states, both within the $4f^{13}$ configuration, not experiencing the bond length changes and subsequent broadening which the interconfigurational absorption bands are subject to. This line is found to be split by about 8 $cm^{-1}$. In octahedral coordination, the lowest energy crystal field components of $^2F_{7/2}$ and $^2F_{5/2}$ are $\Gamma_8$ and $\Gamma_6$ respectively. The 8 $cm^{-1}$ splitting is attributed to a splitting of $^2F_{5/2}$ ($\Gamma_8$) into two Kramer doublets [1, 19].

The 4f-5d features of the absorption spectrum are much broader due to the change in configuration involved in the transitions. The change in configuration also corresponds to Stokes shifts in these absorption bands, while there was no Stokes shift in the 4f-4f absorption features. The weak absorption band centred around 13500 $cm^{-1}$ is absorption into the $(^3H_6,t_{2g})S=1/2$ state [1]. The absorption band centred on about 15000 $cm^{-1}$ is associated with absorption into the $(^3H_6,t_{2g})S=1/2$ state [19]. The absorption band which begins at around 20000 $cm^{-1}$ is associated with absorption into the $(^3F_4,t_{2g})$ state.

It is indicated in figure 3.4 which multiplet, $(^3H_6,t_{2g})$ or $(^3F_4,t_{2g})$, the absorption bands are associated with.

## 3.4 Upconversion Processes

Normally in phosphor materials a sample is excited with higher energy photons than those it is emitting. Upconversion is a process involving a sample emitting photons at a higher energy than those it is being excited with [22], so lower energy photons are being 'converted' to higher energy photons. The comparison between these two processes can be seen in figure 3.5. Here, the left part shows that a single higher energy photon can cause the emission of a photon $A$. In the right part of figure 3.5 two lower energy photons are used to cause the emission $A$, upconverting them from a lower to higher energy.

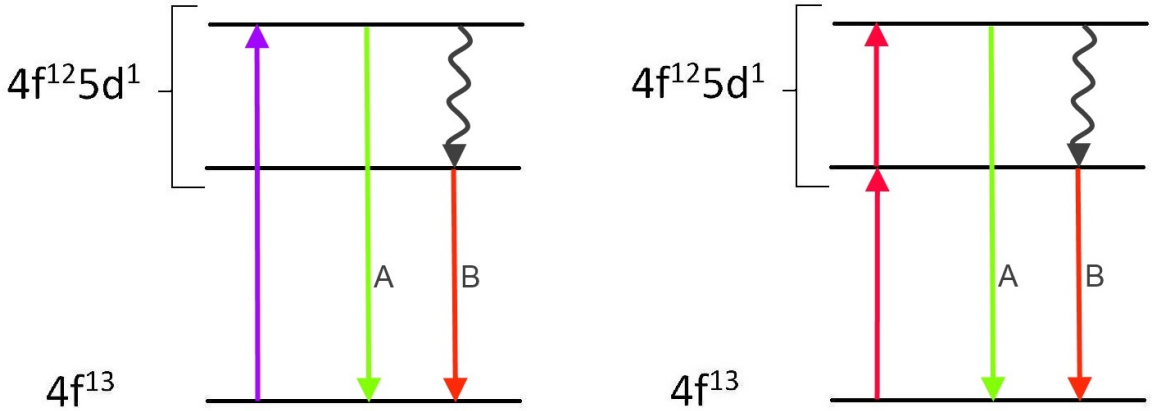


**Figure 3.5** Downconversion versus upconversion. Left: Downconversion, emission 'A' achieved by excitation with higher energy photons. Right: Upconversion, emission 'A' achieved by excitation of multiple lower energy photons.

There are two main types of upconversion process. Ground state absorption/excited state absorption (GSA/ESA) and ground state absorption/energy transfer upconversion (GSA/ETU). Both of these processes require a metastable state to exist between the ground and emitting states [18]. These processes are depicted in figures 3.6 and 3.7. Here we consider upconversion of NIR to UV photons.

The GSA/ESA process is shown in figure 3.6. This process involves an incident NIR photon on the system exciting an electron from the ground to metastable intermediate state. A second NIR photon then excites the electron form the intermediate state to the emitting state, and the system then relaxes radiatively, emitting the upconcerted UV photon [18].

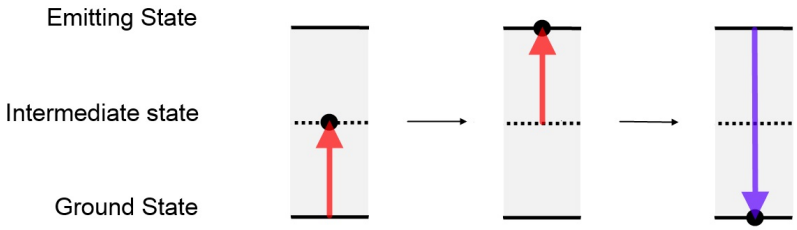


**Figure 3.6** Depiction of ground state absorption/excited state absorption (GSA/ESA) upconversion process.

The GSA/ETU process is shown in figure 3.7. This process involves two emitting sites within the lattice (in this study, two $Tm^{2+}$ sites.) The first step involves two incident NIR photons exciting two electrons on nearby sites so that both are in the metastable intermediate states. The energy from one of the electrons is then transferred to the other, causing one electron to return to the ground state and the other electron to be promoted to the emitting state. The electron in the emitting state then radiatively relaxes, emitting the upconverted UV photon [18].

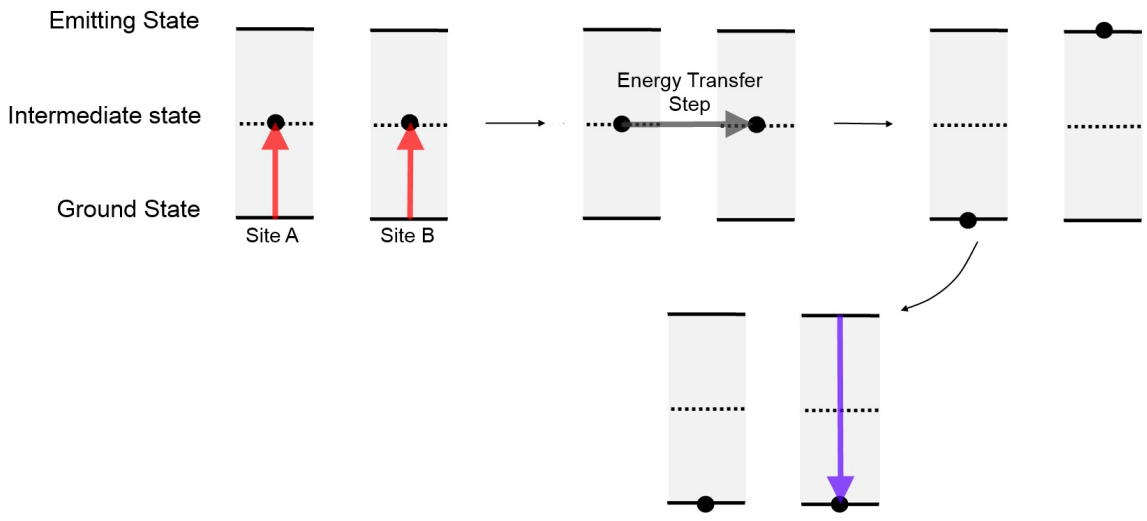


**Figure 3.7** Depiction of ground state absorption/energy transfer upconversion (GSA/ESA) upconversion process.

An efficient upconversion process is found in $Tm^{2+}$ [2, 5]. It is interesting because although upconversion processes are widespread through the lanthanide series within 4f energy levels [2], in $Tm^{2+}$ upconversion emission is observed from a higher 5d state [2]. This is

aided by the low phonon energies of the host lattice, meaning non-radiative emission takes longer to happen and intermediate states in the upconversion process can persist for long enough to be excited to higher energy states, as well as the higher 5d states persisting for long enough to radiatively emit.

# Chapter 4

# Experimental Method

## 4.1 Synthesis of Crystals

All of the crystal samples used ($RbCaI_3$, $CsCaBr_3$, $CsCaCl_3$ and $SrCl_2$) were supplied by the research group of Prof. H. U. Güdel at the University of Bern in Switzerland.

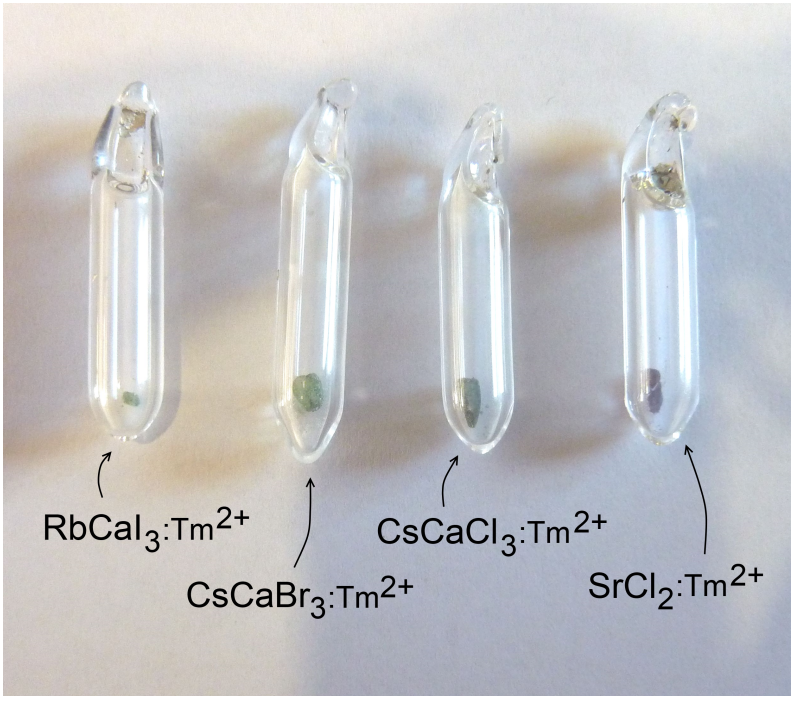


**Figure 4.1** Crystal samples sealed in quartz ampoules with partial He pressure due to their hygroscopic nature. From right to left they are $RbCaI_3$:$Tm^{2+}$, $CsCaBr_3$:$Tm^{2+}$, $CsCaCl_3$:$Tm^{2+}$ and $SrCl_2$:$Tm^{2+}$.

The crystals were grown by the Bridgman technique. This involves heating the materials above their melting point in a container and slowly cooling them back down to room temperature. The cooling is done in such a way so that there is a temperature gradient

across the volume of material present, and the sample is cooled from one end to the other. This allows the crystal structure to slowly build across the entire mass as it cools.

The samples being produced are very hygroscopic which means they absorb water out of the air. This means that during and after synthesis precautions must be taken to prevent the sample having contact with the air. The starting materials were enclosed in tantalum ampoules under partial pressure of He. After being prepared the samples are stored in quartz ampoules with partial pressure of He. The reason for the two types of ampoules is that during synthesis the $Tm^{2+}$ can be oxidised by quartz at high temperatures, which are involved in the synthesis. However quartz is ideal for housing the samples while they are being studied. The ampoules can be seen in figure 4.1.

The crystals sealed in the ampoules in figure 4.1 can be seen to be dark green (with $SrCl_2$:$Tm^{2+}$ slightly darker than the others.) The $CsCaBr_3$:$Tm^{2+}$ and $CsCaCl_3$:$Tm^{2+}$ crystals are about 2 mm in diameter, and the $RbCaI_3$:$Tm^{2+}$ and $SrCl_2$:$Tm^{2+}$ crystals are about 0.5 mm to 1 mm in diameter. They all have a concentration of 1% $Tm^{2+}$.

## 4.2 Fluorescent Lifetime Measurements

Measurements of fluorescence decay were taken after the samples were optically excited by a pulsed laser. From these measurements the lifetimes could be found. For each observed band, measurements were taken at a range of temperatures to see how temperature affected the transitions. The experimental setup for taking these measurements is shown in figure 4.2.

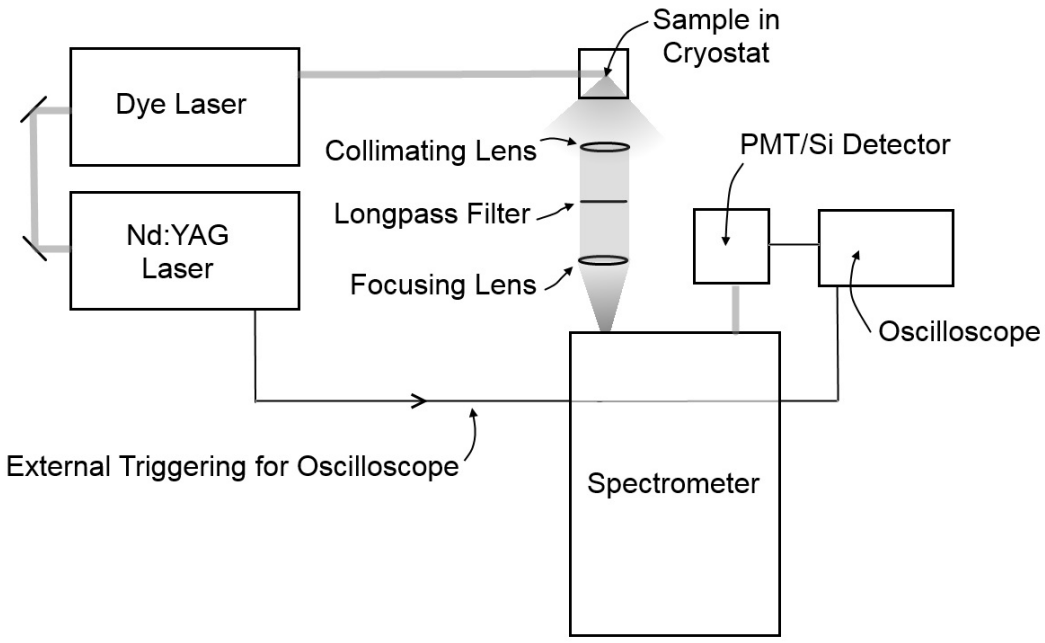


**Figure 4.2** Experimental setup for measuring fluorescence decay. A pulsed dye laser is used to generate the beam needed to excite the sample. This dye laser is pumped with a Nd:YAG laser. This beam is then incident on the sample. The sample is contained within a cryostat cooled with liquid helium. The light emitted from the sample is collimated then focused onto the opening of the spectrometer. A longpass filter is placed within the collimated beam. After the beam has passed through the spectrometer, it is incident upon either a PMT or a silicon detector, depending on the wavelength of emission being investigated. The PMT/Si detector then sends a signal to the oscilloscope, which is being externally triggered by the Nd:YAG laser.

A pulsed dye laser is used to generate the beam needed to excite the sample. This dye laser is pumped with a Nd:YAG laser. This beam is then incident on the sample, it was not necessary to focus the beam onto the sample as plenty of light was emitted without focusing. The sample is contained within a cryostat cooled with liquid helium. The light

emitted from the sample is collimated then focused onto the opening of the spectrometer. A longpass filter is placed within the collimated beam, with a cutoff wavelength such that emission from the sample is able to pass through but any reflected laser light is not. After the beam has passed through the spectrometer, it is incident upon either a photomultiplier tube (PMT) or a silicon detector, depending on the wavelength of emission being investigated. The PMT/Si detector then sends a signal to the oscilloscope, which is being externally triggered by the Nd:YAG laser. Here the measurements of intensity as a function of time are recorded. The temperature is controlled by balancing the flow of helium into the cryostat with the right amount of heating.

For all measurements, a Quanta-ray pro-series pulsed Nd:YAG laser, a Sirah pulsed dye laser, an Oxford Instruments Microstat cryostat, an Acton Spectrapro 2150i spectrometer, and a tektronix TDS 2022 oscilloscope were used.

Infrared emission from $CsCaCl_3$:$Tm^{2+}$ was detected at 12,000 $cm^{-1}$ (833 nm.) The decay was measured from 14 K to 320 K. The detector used for these measurements was a PDA 100A Silicon detector and a 600 nm longpass filter was used to cut out the laser light. The sample was excited with 28,940 $cm^{-1}$ (345 nm) laser light. An attempt was made to measure visible emission from $CsCaCl_3$:$Tm^{2+}$, exciting the sample at 28,940 $cm^{-1}$ (345 nm), however no emission intense enough to be detected was observed.

Visible emission from $CsCaBr_3$:$Tm^{2+}$ was detected at 19,070 $cm^{-1}$ (524 nm) and The decay was measured from 9 K to 270 K. The detector used for these measurements was a Hamamatsu R1547 PMT with a 50 Ω load resistor and a 400 nm longpass filter was used to cut out the laser light. The sample was excited with 28,940 $cm^{-1}$ (345 nm) laser light. Infrared emission from $CsCaBr_3$:$Tm^{2+}$ was detected at 12,270 $cm^{-1}$ (815 nm.) The decay was measured from 10 K to 300 K. The detector used for these measurements was a PDA 100A Silicon detector and a 600 nm longpass filter was used to cut out the laser light. The sample was excited with 28,940 $cm^{-1}$ (345 nm) laser light.

Visible emission from $RbCaI_3$:$Tm^{2+}$ was detected at 17,240 $cm^{-1}$ (580 nm.) The decay was measured from 28 K to 230 K. The detector used for these measurements was a Hamamatsu R1547 PMT with a 50 Ω load resistor and a 400 nm longpass filter was used to cut out the laser light. The sample was excited with 28,940 $cm^{-1}$ (345 nm) laser light.

An attempt was made to measure Infrared emission from $RbCaI_3$:$Tm^{2+}$. The presence of emission at 955 nm when exciting at 28,940 $cm^{-1}$ (345 nm) was noted, however due to equipment problems the fluorescent decay was not able to be recorded.

An attempt was made at measuring visible emission from $SrCl_2$:$Tm^{2+}$, exciting the sample at 28,940 $cm^{-1}$ (345 nm), however no emission intense enough to be detected was observed. An attempt was also made at measuring infrared emission from this sample. The presence of the emission at 715 nm while exciting at 28,940 $cm^{-1}$ (345 nm) was noted, however due to equipment failure the fluorescent decay was not able to be measured.

## Chapter 5

# Optical Properties and Crystal-Field Calculations for $Tm^{2+}$ in $CsCaCl_3$, $CsCaBr_3$ and $CsCaI_3$

The energy structure of the $Tm^{2+}$ ion was examined by performing parametric calculations to simulate absorption spectra of $Tm^{2+}$ in the different materials. These calculations output energy levels and dipole strengths within the ion, allowing insight to the structure. The parameters used to generate the spectra can also provide physical information about the ion. Crystal-field calculations are performed for $CsCaCl_3$, $CsCaBr_3$ and $CsCaI_3$, but not for $RbCaI_3$ as no absorption data was available for comparison.

## 5.1 Energy Level Calculations

Figure 5.1 shows a basic representation of the lower energy levels within the ion. The energy levels of the $4f^{13}$ configuration and the lower levels of the $4f^{12}5d^1$ configuration are shown. The $4f^{13}$ configuration is seen to be split into $^2F_{5/2}$ to $^2F_{7/2}$ states. The $4f^{12}5d^1$ is seen to be split into ($^3F_4$,$t_{2g}$) and ($^3H_6$,$t_{2g}$) states, where the latter is further split into *S=1/2* and *S=3/2* states. The d orbital experiences a crystal field splitting into $e_g$ and $t_{2g}$ states, but only $t_{2g}$ states are shown in figure 5.1.

There are five radiative emissions occurring in the $Tm^{2+}$ ion. Two of them much more intense than the others. These are indicated by the arrows in figure 5.1. Visible emission is observed as a result of a radiative relaxation from ($^3F_4$,$t_{2g}$) and infrared emission is observed as a result of radiative relaxation from ($^3H_6$,$t_{2g}$)*S=3/2*.

Energy levels within the ion are found for the ground ($4f^{13}$) and excited ($4f^{12}5d^1$) configuration by finding the eigenvalues of the Hamiltonians given in equations 5.1 and 5.2. $H$ is the $4f^{12}$ 'core' Hamiltonian and $H_d$ is the Hamiltonian describing the 5d and f-d

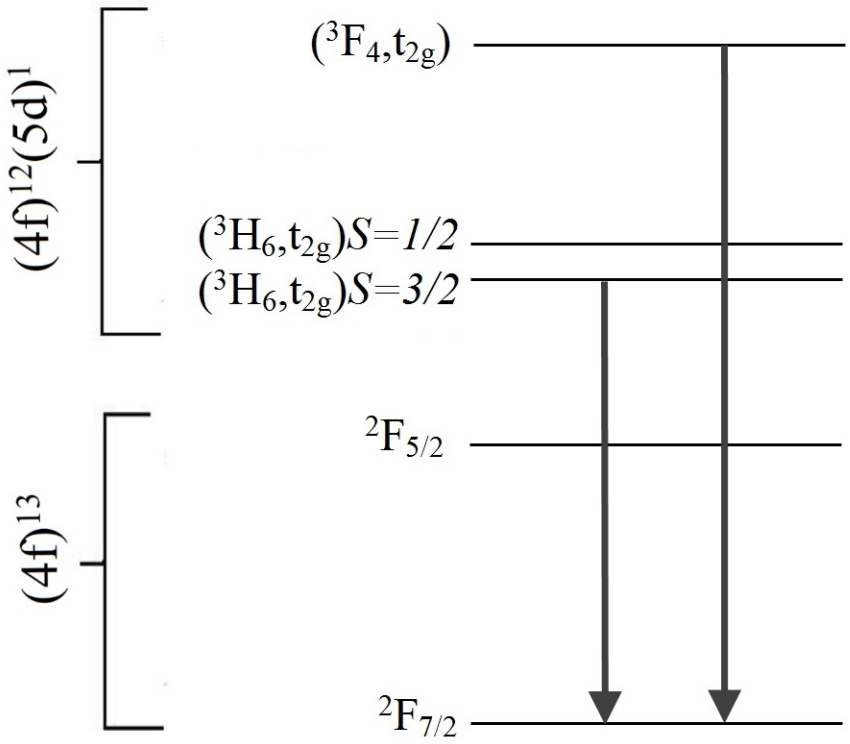


**Figure 5.1** A simple representation of the energy levels within the $Tm^{2+}$ ion. Energy levels within both the $4f^{13}$ and $4f^{12}5d^1$ configurations are shown. The arrows represent radiative emission between some levels.

interactions. The eigenvalues of both Hamiltonians are calculated to output theoretical energy levels within the ion. These are listed in table 5.2.

$$H = E_{avg} + \sum_{k=2,4,6} F^k f_k + \varsigma_f A_{so} + \alpha L(L+1) + \beta G(G_2) + \gamma G(R_7) + \sum_{i=2,3,4,6,7,8} T^i t_i + \sum_{h=0,2,4} M^h m_h + \sum_{k=2,4,6} P^k p_k + \sum_{k,q} B_q^k C_q^{(k)} \quad (5.1)$$

$$H_d = \Delta_E(fd) + \sum_{k=2,4} F^k(fd) f_k(fd) + \sum_{j=1,3,5} G^j(fd) g_j(fd) + \varsigma(dd) A_{so}(d) + \sum_{k=2,4} B_q^k(d) C_q^{(k)}(d) \quad (5.2)$$

The zero phonon lines of absorption transitions are taken as the energy differences between levels. These allow a simulated spectrum to be constructed by plotting Gaussians offset from the zero phonon lines. The intensities of the transitions are taken from the dipole strength of each transition. In this thesis, the simulated spectrum is fitted to the experimental spectrum. This means that the position of the zero phonon lines is found in the process of fitting.

The different parameters involved in constructing the Hamiltonians are described in detail in section 2.1. The parameters for each material are determined by inspecting how each of them changes the simulated absorption spectrum. The simulated and experimental spectra are compared, and the parameters changed until the two spectra match as closely as possible. These parameters are listed in table 5.1

These calculations are performed for the three different materials being considered. The primary difference between these materials is the atomic radii of the anions involved. The ionic radii of $Cl^-$, $Br^-$ and $I^-$ are 167 pm, 182 pm and 206 pm respectively. This change in the lattice environment has an effect on the doped ion, so examining it in these different environments can be useful.

## 5.2 Simulations of the Optical Spectra

As mentioned previously, experimentally acquired absorption spectra are required as a way of measuring the accuracy of the calculated values and simulated spectra. Absorption data for $CsCaCl_3$:$Tm^{2+}$, $CsCaBr_3$:$Tm^{2+}$, and $CsCaI_3$:$Tm^{2+}$ were provided by the research group of Prof. H. U. Güdel at the University of Bern in Switzerland.

This absorption data has a background present, increasing with energy. This is likely due to scattering and absorption in the host, and so not related to the physics of the $Tm^{2+}$ ion. This background intensity was removed by fitting polynomials to the data, and then subtracting these polynomials in order to get the spectra which are used.

When the calculation is performed, the dipole strengths are calculated. The relative strengths of these for different transitions are used to simulate the spectra. The oscillator strength is a more accurate measure of absorption band intensity. Oscillator strength is proportional to the dipole strength multiplied by the energy. This means that if oscillator strengths were used, the simulated spectra would experience an increase in intensity of absorption features at higher energies. This would ordinarily mean an adjustment is required to the simulated spectra in order for it to agree with the experimental data. The scattering background previously mentioned appears to have decreased the intensity of the absorption peaks at high energies, so subtracting this background also accounted for the difference between the dipole and oscillator strengths.

Absorption spectra were simulated for $CsCaCl_3$:$Tm^{2+}$, $CsCaBr_3$:$Tm^{2+}$ and $CsCaI_3$:$Tm^{2+}$. The simulations were limited to these materials as they were the only materials for which experimental absorption data was available for comparison.

To produce the spectra, Gaussians of width 700 $cm^{-1}$ were used, displaced from the zero phonon lines by 300 $cm^{-1}$. The simulated spectra were qualitatively fitted to the experimental data. The parameters for each material were determined by observing the effect of changing them on the shape of each simulated spectrum, then making the appropriate changes to the parameters.

Comparisons between simulated and experimental spectra are shown in figure 5.2. Simulated and experimental spectra are shown for $CsCaCl_3$:$Tm^{2+}$, $CsCaBr_3$:$Tm^{2+}$ and $CsCaI_3$:$Tm^{2+}$.

In $CsCaCl_3$:$Tm^{2+}$ very good agreement was achieved between the experimental and simulated spectra. The major features can all be seen in both, although there are slight differences in the shapes and relative intensities of some features. In $CsCaBr_3$:$Tm^{2+}$ the main features are again present in both the simulated and experimental spectra, however in this case the relative intensities and precise energies of some features are not quite so similar as in $CsCaCl_3$:$Tm^{2+}$. In $CsCaI_3$:$Tm^{2+}$ once again the main features are all present in both spectra, but some of the relative intensities and precise positions of features do not quite agree. In all cases the best fit as a whole, throughout all energies was sought.

The parameter values for the effective Hamiltonians of $Tm^{2+}$ doped into the host materials $CsCaI_3$, $CsCaBr_3$ and $CsCaCl_3$ are listed in table 5.1, along with the parameters for $SrCl_2$ [23]. The $CsCaI_3$:$Tm^{2+}$, $CsCaBr_3$:$Tm^{2+}$ and $CsCaCl_3$:$Tm^{2+}$ parameters were determined by making changes to those of $SrCl_2$. Parameters for ab inito calculations for $CsCaBr_3$ and $SrCl_2$ with $Yb^{2+}$ doped into it are also shown [24, 25]. There are fewer parameters for the $Yb^{2+}$ doped materials because in this case there is only one hole present in the f orbital when the ion is in its excited state ($4f^{13}5d^1$). This can be seen as equivalent to only one electron being present, so that there are no terms for interactions between f electrons.

The main changes between the $CsCaI_3$:$Tm^{2+}$, $CsCaBr_3$:$Tm^{2+}$ and $CsCaCl_3$:$Tm^{2+}$ spectra came from the parameters $E_{exc}$, $F^2(fd)$, $\zeta(ff)$ and $B_0^4(dd)$.

Many of the parameters were left the same between the three materials. This is due to those parameters having a negligible effect on the shape of the simulated spectra, making selecting the most appropriate values in each of the materials not physically meaningful.

When compared to $SrCl_2$:$Tm^{2+}$, the parameters for $CsCaI_3$:$Tm^{2+}$, $CsCaBr_3$:$Tm^{2+}$ and $CsCaCl_3$:$Tm^{2+}$ are generally quite similar. A notable difference is that the sign of the parameters $B_0^4$ , $B_0^6$, $B_0^4(ff)$, $B_0^6(ff)$ and $B_0^4(dd)$ are opposite to those of $SrCl_2$. This is because $Tm^{2+}$ in $SrCl_2$ has a coordination number of 8, meaning that it has 8 nearest

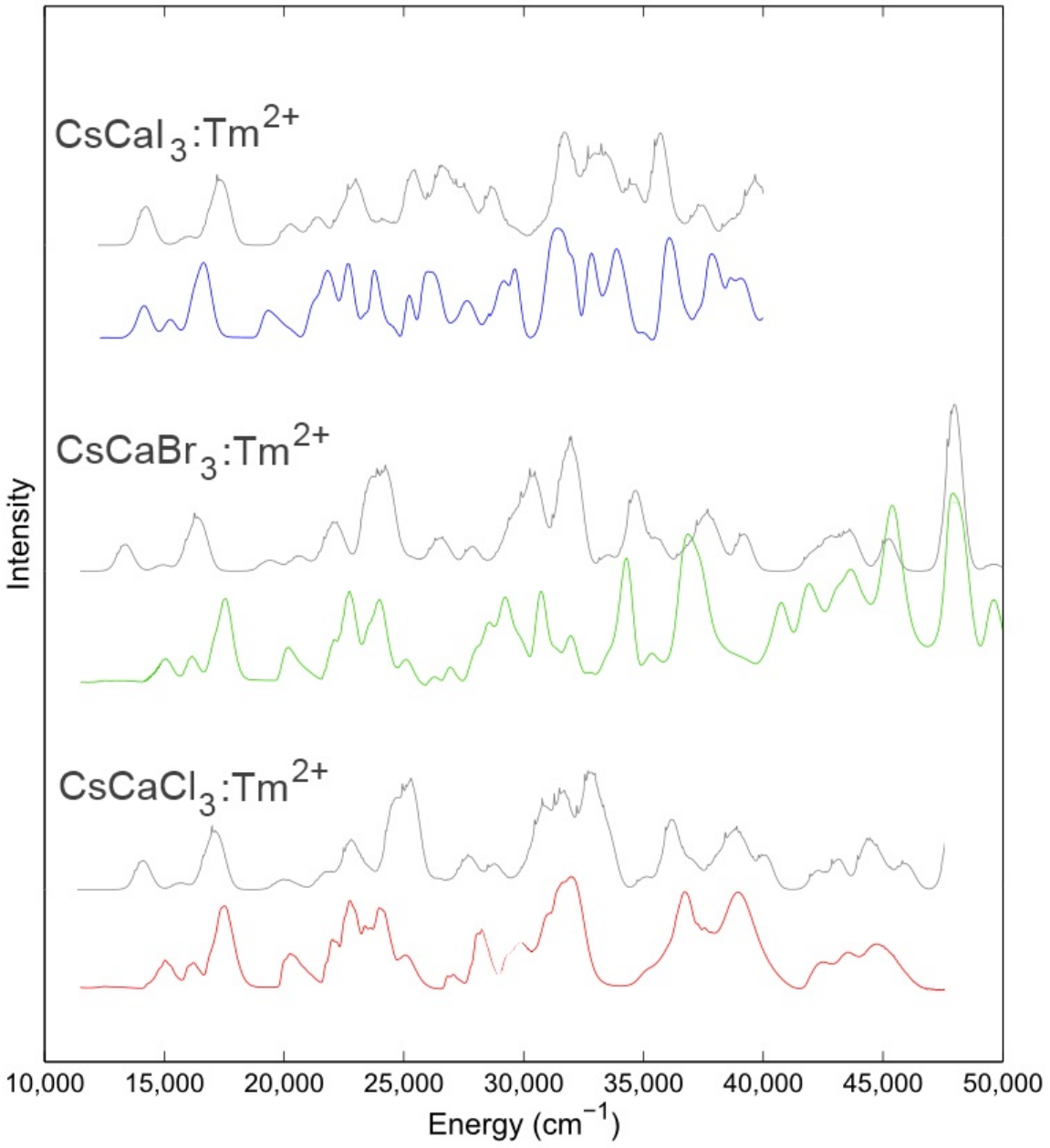


**Figure 5.2** The simulated absorption spectra (grey) for $CsCaI_3$:$Tm^{2+}$, $CsCaBr_3$:$Tm^{2+}$ and $CsCaCl_3$:$Tm^{2+}$ compared to the 10 K experimentally obtained absorption spectra (blue, green and red respectively.) Good agreement of prominent features between the experimental and simulated spectra can be observed for all three materials.

| **Parameter** | **$SrCl_2$:$Yb^{2+}$ (Ab initio)** | **$SrCl_2$:$Tm^{2+}$ (Fitted)** | **$CsCaI_3$:$Tm^{2+}$ (Fitted)** | **$CsCaBr_3$:$Tm^{2+}$ (Fitted)** | **$CsCaCl_3$:$Tm^{2+}$ (Fitted)** | **$CsCaBr_3$:$Yb^{2+}$ (Ab initio)** |
|---|---|---|---|---|---|---|
| $E_{exc}$ | 41802 | 36674 | 33000 | 31800 | 32600 | 39793 |
| $\zeta$ | | 2501 | 2508 | 2508 | 2508 | |
| $B_0^4$ | -194 | -725 | 616 | 616 | 616 | 1381 |
| $B_0^6$ | -592 | 292 | -238 | -238 | -238 | -187 |
| $F^2(ff)$ | | 100429 | 103743 | 105743 | 100743 | |
| $F^4(ff)$ | | 66810 | 71009 | 71009 | 71009 | |
| $F^6(ff)$ | | 56140 | 59669 | 59669 | 59669 | |
| $\alpha(ff)$ | | 17.7 | 18.78 | 18.78 | 18.78 | |
| $\beta(ff)$ | | -626 | -665.7 | -665.7 | -665.7 | |
| $\gamma(ff)$ | | 1825 | 1940 | 1940 | 1940 | |
| $T^2(ff)$ | | 401 | 426 | 426 | 426 | |
| $F^2(fd)$ | 18393 | 14480 | 15805 | 13805 | 13805 | 16795 |
| $F^4(fd)$ | 13099 | 6680 | 6371 | 6371 | 6371 | 9489 |
| $G^1(fd)$ | 5408 | 5912 | 4343 | 4243 | 4243 | 4331 |
| $G^3(fd)$ | 8901 | 4740 | 2463 | 2463 | 2463 | 6947 |
| $G^5(fd)$ | 7165 | 3589 | 1882 | 1882 | 1882 | 7511 |
| $\zeta(ff)$ | 2939 | 2674 | 2358 | 2408 | 2558 | 2939 |
| $\zeta(dd)$ | 1166 | 1050 | 1029 | 1029 | 1029 | 1166 |
| $M^0(ff)$ | | 3.81 | 3.81 | 3.81 | 3.81 | |
| $P^2(ff)$ | | 695 | 695 | 695 | 695 | |
| $B_0^4(ff)$ | | -725 | 616 | 616 | 616 | |
| $B_0^6(ff)$ | | 292 | -238 | -238 | -238 | |
| $B_0^4(dd)$ | -20100 | -19333 | 20000 | 17200 | 17800 | 39639 |

**Table 5.1** Hamiltonian parameter values. Fitted parameters listed for $CsCaI_3$:$Tm^{2+}$, $CsCaBr_3$:$Tm^{2+}$, and $CsCaCl_3$:$Tm^{2+}$ as determined in this thesis. Fitted parameters for $SrCl_2$:$Tm^{2+}$ [23]. Ab initio parameters listed for $SrCl_2$:$Yb^{2+}$ and $CsCaBr_3$:$Yb^{2+}$ [24, 25]. Due to the approximately octahedral coordination of the $Tm^{2+}$ ion, not all the crystal parameters are listed, as $B_4^4 = \sqrt{5/14}B_0^4$ and $B_4^6 = -\sqrt{7/2}B_0^6$.

neighbour atoms within the material. $Tm^{2+}$ in $CsCaI_3$, $CsCaBr_3$, and $CsCaCl_3$ however has a coordination number of 6 meaning that it has 6 nearest neighbour atoms within the material. This can be seen in figures 3.2 and 3.1. The different geometries are of importance when calculating the crystal field parameters, and result in crystal field parameters of opposite signs for the different types of materials.

When compared to $CsCaBr_3$:$Yb^{2+}$, the parameters for $CsCaI_3$:$Tm^{2+}$, $CsCaBr_3$:$Tm^{2+}$ and $CsCaCl_3$:$Tm^{2+}$ should be similar, however there is the difference of the parameter $B_0^4(dd)$ being approximately twice as big in the ab initio calculation. The ab initio and fitted parameters for $SrCl_2$ with $Yb^{2+}$ and $Tm^{2+}$ however, are quite similar indicating that the two processes can give similar results.

The first 55 energy levels calculated for all three materials are listed in table 5.2. Along with the energy levels, the dipole strengths associated with absorption into these levels is listed. The energy levels are shown up to just above 20,000 $cm^{-1}$, and experimentally measured absorption bands can be identified by these calculated energy levels.

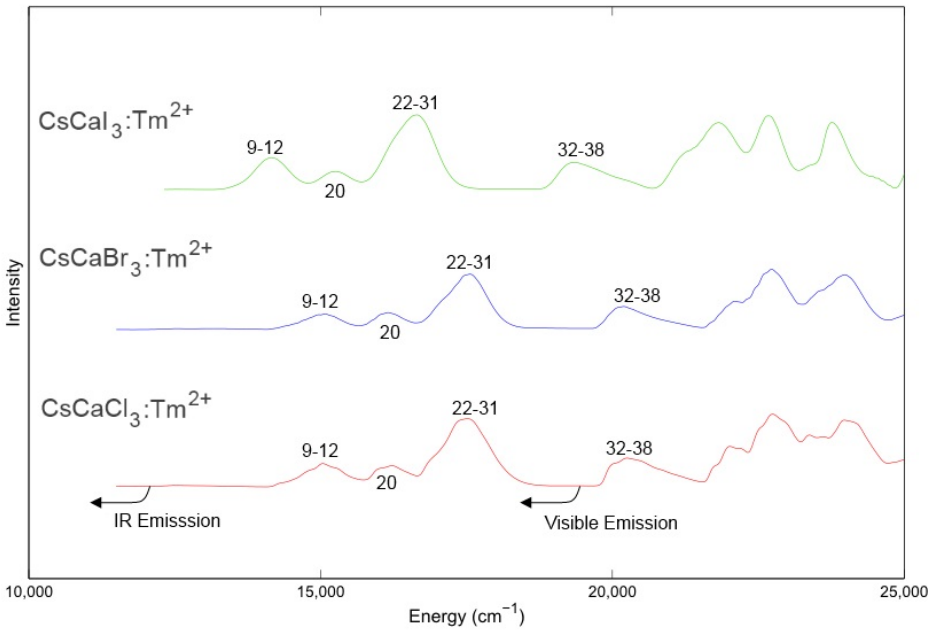


**Figure 5.3** The numbered energy levels from table 5.2 corresponding to absorption features for $CsCaI_3$:$Tm^{2+}$, $CsCaBr_3$:$Tm^{2+}$ and $CsCaCl_3$:$Tm^{2+}$ are indicated on the experimental spectra. The position of visible and IR emissions is also indicated for the case of $CsCaCl_3$:$Tm^{2+}$.

Figure 5.3 shows the experimental absorption spectra for $CsCaI_3:Tm^{2+}$, $CsCaBr_3:Tm^{2+}$ and $CsCaCl_3:Tm^{2+}$. Marked on each of the absorption peaks are the numbered states from table 5.2 which correspond to these absorption bands.

The lowest energy absorption bands seen start at around 15,000 $cm^{-1}$, however in table 5.2 it can be seen that there exist states at lower energy than this. Absorption is not seen into these states on the spectra as it is very weak.

The lowest absorption band marks the beginning of absorption into the ($^3H_6$,$t_{2g}$) states. This is seen at 14,160 $cm^{-1}$ in $CsCaI_3:Tm^{2+}$, 15,070 $cm^{-1}$ in $CsCaBr_3:Tm^{2+}$, and 15,050 $cm^{-1}$ in $CsCaCl_3:Tm^{2+}$. It corresponds to states 10-12 in table 5.2. These states are associated with high dipole strengths up to $24\times10^{-20}$.

The next absorption band, at 15,260 $cm^{-1}$ in $CsCaI_3:Tm^{2+}$, 16,160 $cm^{-1}$ in $CsCaBr_3:Tm^{2+}$, and 16,160 $cm^{-1}$ in $CsCaCl_3:Tm^{2+}$ corresponds to state 20 in table 5.2. This transition has much weaker dipole strengths of up to $6\times10^{-20}$. The strength of this absorption band is underestimated by the calculation.

The next absorption band marks the end of absorption into the ($^3H_6$,$t_{2g}$) states. It is seen at 16,650 $cm^{-1}$ in $CsCaI_3:Tm^{2+}$, 17,570 $cm^{-1}$ in $CsCaBr_3:Tm^{2+}$, and 17,510 $cm^{-1}$ in $CsCaCl_3:Tm^{2+}$ and corresponds to states 23-31 in table 5.2. These levels are associated with very strong dipole strengths up to $60\times10^{-20}$.

The final labeled absorption band is marking the beginning of absorption into the ($^3F_4$,$t_{2g}$) state. It occurs at 19,560 $cm^{-1}$ in $CsCaI_3:Tm^{2+}$, 20,100 $cm^{-1}$ in $CsCaBr_3:Tm^{2+}$, and 20,120 $cm^{-1}$ in $CsCaCl_3:Tm^{2+}$. It corresponds to states 32-38 in table 5.2. These levels are associated with dipole strengths of up to $12\times10^{-20}$.

Also shown in figure 5.3 are the energies at which both visible and IR emission are observed. These energies correspond to the gaps in table 5.2. They occur at places where there is a large enough energy gap between two states such that the relaxation between them will not be purely non-radiative.

| | **$CsCaCl_3$:$Tm^{2+}$** | | **$CsCaBr_3$:$Tm^{2+}$** | | **$CsCaI_3$:$Tm^{2+}$** | |
|---|---|---|---|---|---|---|
| **No.** | **Calculated Energy $cm^{-1}$** | **Isotropic Dipole Strength ($\times 10^{-20}$)** | **Calculated Energy $cm^{-1}$** | **Isotropic Dipole Strength ($\times 10^{-20}$)** | **Calculated Energy $cm^{-1}$** | **Isotropic Dipole Strength ($\times 10^{-20}$)** |
| 1 | 0 | 0.01083 | 0 | 0.01083 | 0 | 0.01083 |
| 2 | 4 | 0.01579 | 4 | 0.01579 | 4 | 0.01579 |
| 3 | 233 | 0.14709 | 233 | 0.14709 | 233 | 0.14709 |
| 4 | 8780 | 0.00764 | 8780 | 0.00764 | 8780 | 0.00764 |
| 5 | 8961 | 0.00212 | 8961 | 0.00212 | 8961 | 0.00212 |
| 6 | 12366 | 0.00558 | 11638 | 0.00361 | 12350 | 0.01035 |
| 7 | 12516 | 0.00223 | 11787 | 0.00657 | 12508 | 0.00088 |
| 8 | 12534 | 0.00573 | 11803 | 0.00282 | 12524 | 0.01253 |
| 9 | 13621 | 4.03893 | 12882 | 3.93688 | 13757 | 4.50086 |
| 10 | 13721 | 7.69955 | 12980 | 7.4042 | 13827 | 8.95375 |
| 11 | 13779 | 21.1693 | 13038 | 20.4069 | 13910 | 23.6333 |
| 12 | 13937 | 15.6287 | 13196 | 15.1767 | 14031 | 16.7836 |
| 13 | 14009 | 1.36844 | 13266 | 1.3688 | 14132 | 1.10853 |
| 14 | 14034 | 0.10623 | 13307 | 0.09619 | 14192 | 0.06181 |
| 15 | 14082 | 0.88878 | 13353 | 0.67694 | 14240 | 1.46746 |
| 16 | 14100 | 0.43669 | 13372 | 0.37223 | 14259 | 0.43285 |
| 17 | 14310 | 0.35676 | 13580 | 0.3387 | 14546 | 0.43689 |
| 18 | 15019 | 0.42036 | 14290 | 0.39658 | 15302 | 0.49401 |
| 19 | 15135 | 0.77992 | 14404 | 0.75111 | 15432 | 0.84298 |
| 20 | 15347 | 5.88935 | 14614 | 5.75755 | 15658 | 6.1204 |
| 21 | 15391 | 0.01608 | 14658 | 0.0188 | 15710 | 0.0176 |
| 22 | 15489 | 4.41224 | 14751 | 4.27495 | 15837 | 5.3736 |
| 23 | 16324 | 8.4287 | 15587 | 8.55605 | 16628 | 13.9247 |
| 24 | 16434 | 3.90678 | 15703 | 4.38396 | 16783 | 4.78984 |
| 25 | 16438 | 0.00196 | 15709 | 0.01114 | 16784 | 3.48617 |
| 26 | 16457 | 3.33089 | 15729 | 3.65432 | 16790 | 8.7928 |
| 27 | 16565 | 10.3966 | 15841 | 9.82925 | 16798 | 3.97001 |
| 28 | 16575 | 10.3742 | 15856 | 9.67395 | 16819 | 2.54939 |
| 29 | 16620 | 24.0828 | 15896 | 22.2863 | 16850 | 14.7689 |
| 30 | 16989 | 59.7435 | 16263 | 57.309 | 17201 | 57.0145 |
| 31 | 17117 | 10.1696 | 16382 | 9.76705 | 17300 | 10.3484 |
| 32 | 19494 | 6.60925 | 18925 | 6.77845 | 19855 | 11.1261 |
| 33 | 19581 | 3.14366 | 18988 | 3.83224 | 19879 | 6.089 |
| 34 | 19718 | 3.03317 | 19077 | 4.58801 | 19923 | 7.15045 |
| 35 | 19824 | 0.01856 | 19258 | 1.33188 | 20133 | 1.90983 |
| 36 | 19841 | 1.37293 | 19366 | 1.3373 | 20151 | 0.2022 |

| | | | | | | |
|---|---|---|---|---|---|---|
| 37 | 19923 | 1.35072 | 19425 | 2.58191 | 20289 | 2.24513 |
| 38 | 19964 | 3.00721 | 19552 | 2.24184 | 20323 | 2.33488 |
| 39 | 20206 | 0.05895 | 19612 | 1.71279 | 20395 | 1.46446 |
| 40 | 20217 | 3.35677 | 19616 | 0.12265 | 20494 | 2.38676 |
| 41 | 20256 | 1.29247 | 19816 | 0.00792 | 20528 | 1.22749 |
| 42 | 20459 | 0.36675 | 19825 | 0.27805 | 20777 | 0.8759 |
| 43 | 20468 | 0.20242 | 20157 | 0.95908 | 20779 | 0.35123 |
| 44 | 21204 | 1.83043 | 20185 | 7.9567 | 20931 | 0.04866 |
| 45 | 21247 | 0.8597 | 20190 | 0.03852 | 20962 | 0.6066 |
| 46 | 21291 | 0.08314 | 20212 | 1.32085 | 20984 | 8.9914 |
| 47 | 21304 | 7.58175 | 20247 | 3.35791 | 21024 | 1.91568 |
| 48 | 21352 | 4.94543 | 20296 | 0.11902 | 21042 | 3.17889 |
| 49 | 21470 | 0.0698 | 20424 | 9.2782 | 21094 | 2.8286 |
| 50 | 21493 | 5.89375 | 20542 | 5.3516 | 21189 | 13.1311 |
| 51 | 21642 | 5.37585 | 20847 | 0.86386 | 21289 | 9.3542 |
| 52 | 21714 | 4.95773 | 20976 | 0.11226 | 21857 | 0.58634 |
| 53 | 21939 | 1.06488 | 21086 | 4.046 | 22053 | 14.0789 |
| 54 | 21945 | 0.00723 | 21173 | 1.4835 | 22076 | 17.3727 |
| 55 | 21964 | 4.89009 | 21231 | 3.30393 | 22169 | 3.29833 |

**Table 5.2** Calculated energies of the first 55 states of $CsCaCl_3:Tm^{2+}$, $CsCaBr_3:Tm^{2+}$, and $CsCaI_3:Tm^{2+}$. Shown along with the energy levels are the isotropic dipole strengths of absorption into each state.

## Chapter 6

# Temperature Dependent Fluorescence Lifetimes

Examining the relationship between fluorescence lifetime and temperature in a crystal system can give insight into relaxation processes. Here a multiphonon model and a phonon assisted barrier hopping model will be explored, and applied to experimental data obtained. This analysis was performed on $CsCaCl_3:Tm^{2+}$, $CsCaBr_3:Tm^{2+}$ and $RbCaI_3:Tm^{2+}$, but as no crystal sample of $CsCaI_3:Tm^{2+}$ was available, it could not be analysed in this way.

The multiphonon model examines the relationship between emissions from the same state. Radiative emission, and non-radiative relaxation in the form of a cascade of phonons are the types of emissions considered here. The interplay of these factors at varying temperature will be explored. The phonon assisted barrier hopping model again examined the interplay of radiative emission and non-radiative relaxation, this time in the form of phonons overcoming a potential barrier in order to non-radiatively relax. The parameters output from fitting these models to experimental data will give insight into the systems being examined.

Before the lifetime can be analysed as a function of temperature, it is required that lifetimes be extracted from the data collected. At each temperature, the intensity of emission as a function of time immediately after excitation was recorded. The decay curves which resulted from this can be seen in figure 6.1 for all temperatures in $CsCaCl_3:Tm^{2+}$.

In figure 6.1 the decay curves are plotted with both a linear and a log intensity scale. The value of the log scale is that given the straight line nature of the curves on this scale, it can be deduced that a single exponential can reasonably be fit to the data to obtain the lifetime of the emission.

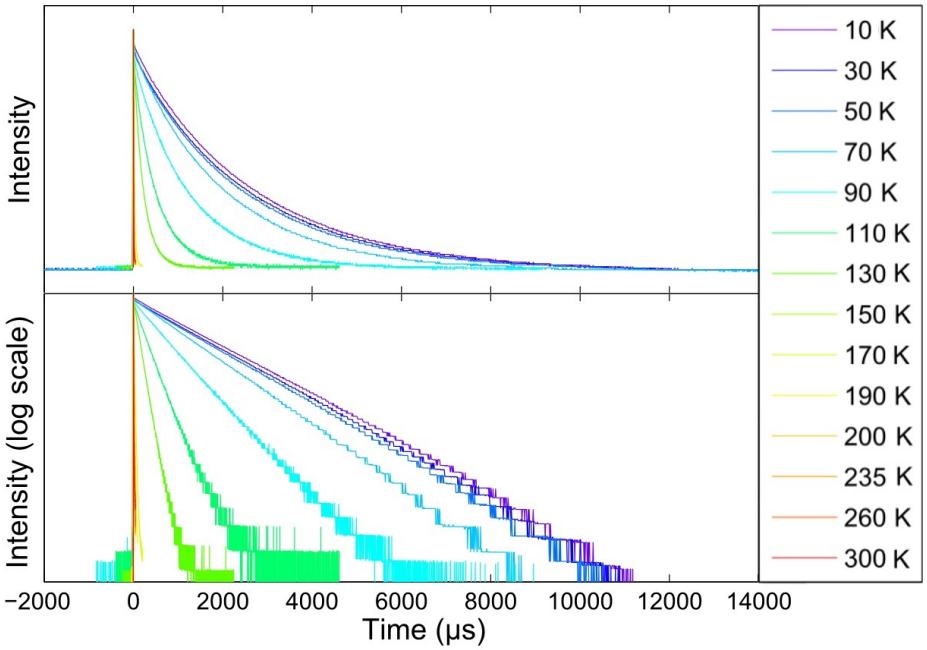


**Figure 6.1** Decay curves for $CsCaCl_3:Tm^{2+}$ from 10 K to 300 K. Curves are displayed with both a linear (top) and a log (bottom) intensity scale. IR emission band at 12,000 $cm^{-1}$ (833 nm) being monitored. Sample excited at 28,940 $cm^{-1}$ (345 nm.)

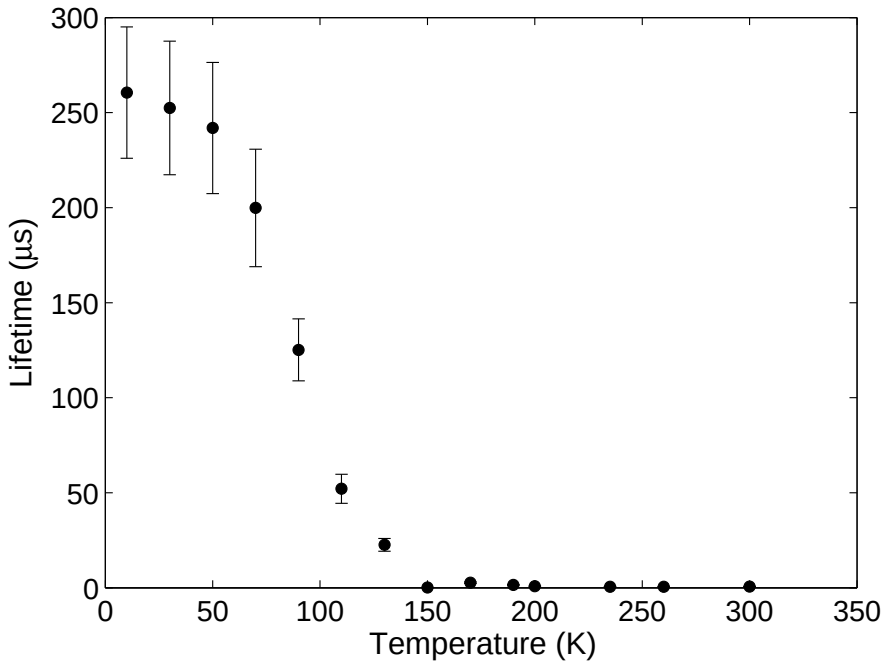


**Figure 6.2** Lifetime as a function of temperature determined from decay data measured for $CsCaCl_3:Tm^{2+}$. IR emission band at 12,000 $cm^{-1}$ (833 nm) is being monitored. Sample excited at 28,940 $cm^{-1}$ (345 nm.)

Equation 6.1, a single exponential, is fit to the experimental data. The lifetime obtained for each temperature is shown in figure 6.2, along with the uncertainties for each point.

$$I(t) = I(0)\exp(-t/\tau) \tag{6.1}$$

The data was fit using a least squares fitting regime. This means that the sum of the squares of the residuals between the data and the model, $S$ in equation 6.2 were minimised. The uncertainties seen were calculated from the Hessian matrix.

$$S = \sum_{i=1}^{n}(y_i - f(x_i))^2 \tag{6.2}$$

This process was applied to all emissions measured. The data in the form seen in figure 6.2 is now able to have further analysis performed on it. Both the multiphonon and barrier models discussed in section 2.2 will be fit to data acquired for lifetime as a function of temperature.

## 6.1 Direct Multiphonon Relaxation

The first model to be implemented is the multiphonon model described in section 2.2.1. This model considers a cascade of phonons of energy $\hbar\omega$ bridging an energy gap $\Delta E$. In the case of $Tm^{2+}$ this is the energy gap between the ($^3F_4$,$t_{2g}$) and ($^3H_6$,$t_{2g}$) states, as seen by the curly arrows in figure 6.3.

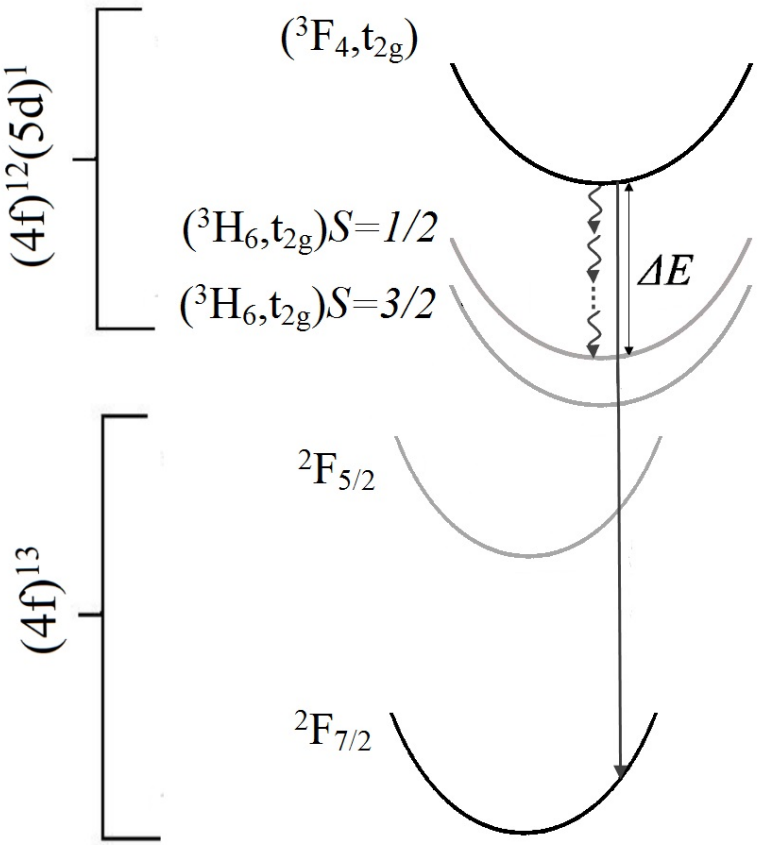


**Figure 6.3** A configurational coordinate diagram of the energy levels within the $Tm^{2+}$ ion. Energy levels within both the $(4f)^{13}$ and $(4f)^{12}(5d)^1$ configurations are shown. The radiative emission being monitored here is shown with a straight arrow between bold levels. The competing phonon cascade is represented with curly arrows. The energy gap to be bridged with phonons is labeled $\Delta E$.

The model of experimental lifetime changing with temperature derived from this idea

explores the competition between the radiative emission and the multiphonon relaxation from the ($^3$F$_4$,t$_{2g}$) level. The equation which describes this, and which is fitted to experimental data is equation 6.3.

$$\tau_{exp}(T) = \frac{1}{\left(\tau_{nr}(0)\left[1-\exp\left(\frac{\hbar\omega_{eff}}{k_B T}\right)\right]^N\right)^{-1} + \frac{1}{\tau_r}} \tag{6.3}$$

Here $\tau_{nr}(T)$ is the non-radiative lifetime as a function of temperature, $\tau_{nr}(0)$ is the non-radiative lifetime at 0 K, $\tau_r$ is the radiative lifetime, $\hbar\omega_{eff}$ is the energy of the effective phonon modes involved, $k_B$ is Boltzmann's constant, $T$ is the temperature in Kelvin, and $N$ is the number of phonons needed to bridge the energy gap.

Experimental data was available for both visible and IR emission. Equation 6.3 describes a radiative relaxation and a multiphonon cascade as competing processes from the same original state. In the case of visible emission this can be clearly seen to be the case in figure 6.3, with the two processes originating from the ($^3$F$_4$,t$_{2g}$) state, and so this multiphonon model is applied successfully to this emission. In the case of the IR emission however, the radiative emission is originating from the ($^3$H$_6$,t$_{2g}$)$S = 3/2$ state, which is the lowest state of the excited configuration. This means that any multiphonon relaxation would involve a configurational shift, which is not well modelled by equation 6.3. IR emission is therefore not modelled using this method.

As with the fitting of the decay curves, equation 6.3 was fit to the lifetime data as a function of temperature using a least squares fitting regime. The parameters allowed to vary were $\tau_{nr}(0)$, $\tau_r$, $\hbar\omega_{eff}$, and $N$. The output parameters are listed in table 6.1. The fittted model is compared to experimental data in figures 6.4 for $CsCaBr_3$:$Tm^{2+}$ and 6.5 for $RbCaI_3$:$Tm^{2+}$.

In the case of $CsCaBr_3$:$Tm^{2+}$, in figure 6.4, a very good fit to the experimental data is achieved. The lifetime can be seen to be steady at around 1.7 $\mu s$ up until 50 K where the lifetime begins to decrease. The emission is completely quenched by 125 K. In the case of $RbCaI_3$:$Tm^{2+}$, in figure 6.5 a good fit is achieved for most temperatures, but not so

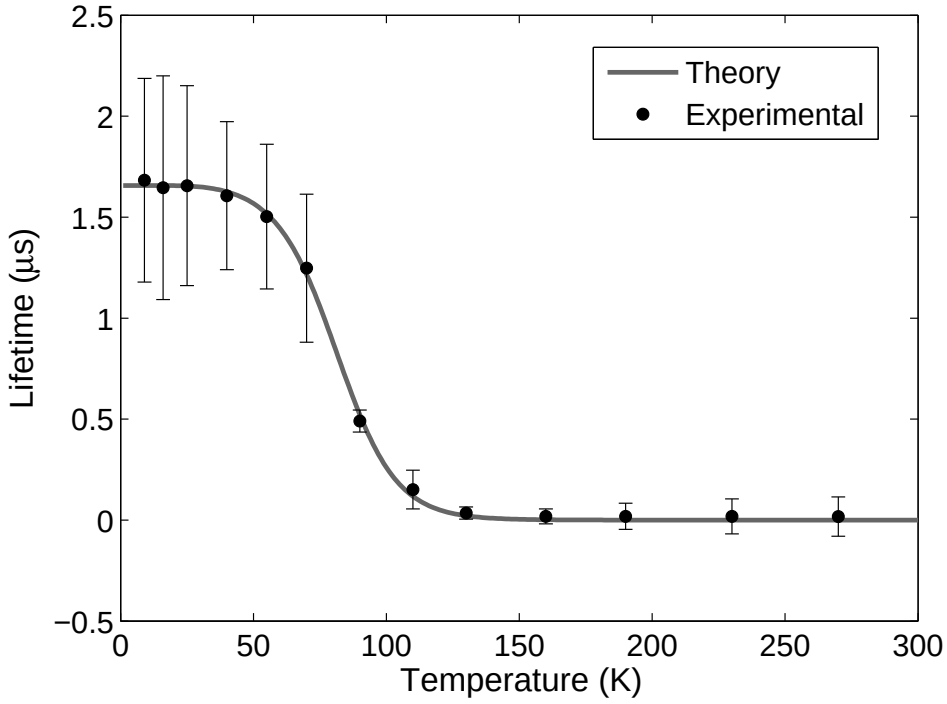


**Figure 6.4** Multiphonon model fitted to lifetime data for $CsCaBr_3:Tm^{2+}$. Visible emission band at 19,070 $cm^{-1}$ (524 nm) being monitored. Sample excited at 28,940 $cm^{-1}$ (345 nm.)

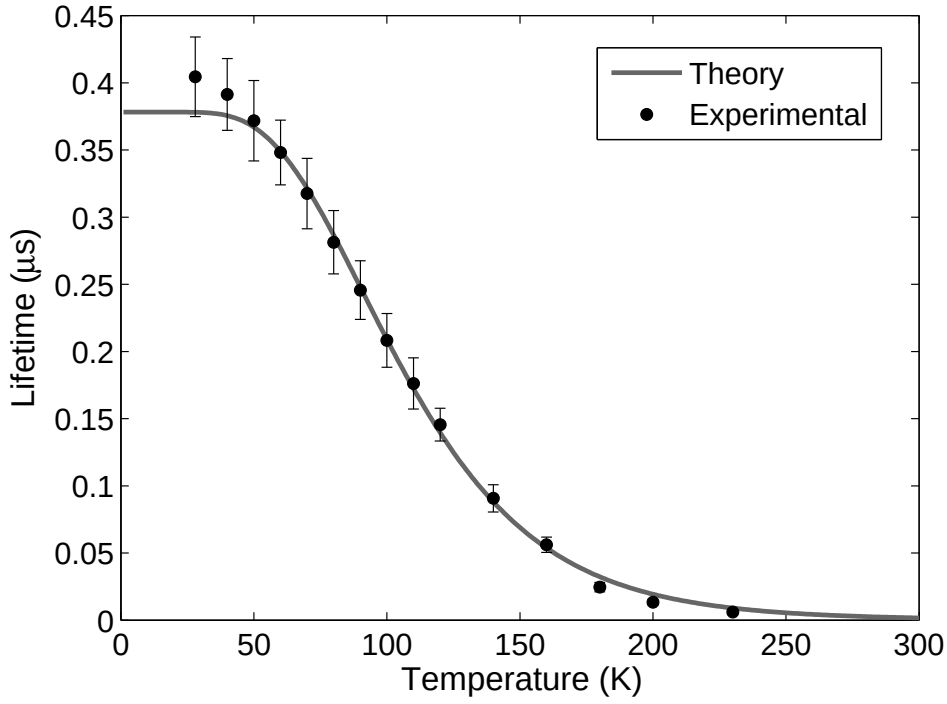


**Figure 6.5** Multiphonon model fitted to lifetime data for $RbCaI_3:Tm^{2+}$. Visible emission band at 17,240 $cm^{-1}$ (580 nm) being monitored. Sample excited at 28,940 $cm^{-1}$ (345 nm.)

| **Parameter** | **$CsCaBr_3$:$Tm^{2+}$** | **$RbCaI_3$:$Tm^{2+}$** |
|---|---|---|
| $\hbar\omega(cm^{-1})$ | 113 | 204 |
| N | 22 | 12 |
| $\tau_r$ ($\mu s$) | 1.73 | 3.80 |
| $\tau_{nr}(0)$ ($\mu s$) | 41 | 0.42 |

**Table 6.1** Fitted values of parameters in the multiphonon model described by equation 6.3 for visible emission from $CsCaBr_3$:$Tm^{2+}$ and $RbCaI_3$:$Tm^{2+}$.

well for very low temperatures. The lifetime at the lowest temperature measured (28 K) is 0.40 $\mu s$, however the low temperature region of steady lifetime seen for $CsCaBr_3$:$Tm^{2+}$ does not appear to be present so strongly in this data. The lifetime again has almost completely died away by 225 K.

The size of the energy gap being bridged ($\Delta E$) can be determined by multiplying the energy of the phonons ($\hbar\omega$) by the number of phonons $N$. This results in a value of $\Delta E = 2486$ cm$^{-1}$ for $CsCaBr_3$:$Tm^{2+}$ and $\Delta E = 2448$ cm$^{-1}$ for $RbCaI_3$:$Tm^{2+}$. The size of this gap can be determined from the absorption spectrum of $CsCaBr_3$:$Tm^{2+}$ as the gap between the highest energy absorption band corresponding to ($^3H_6$,$t_{2g}$) states and the lowest energy absorption band corresponding to ($^3F_4$,$t_{2g}$) states. This value is found to be $\Delta E = 2630$ cm$^{-1}$, so the values from the model are consistent with measured data. The notable difference between the two materials here is that in $CsCaBr_3$:$Tm^{2+}$ there were 22 phonons of energy 113 cm$^{-1}$, and in $RbCaI_3$:$Tm^{2+}$ there were 12 phonons of energy 204 cm$^{-1}$. So $RbCaI_3$:$Tm^{2+}$ has half the phonons, of twice the energy.

The relative sizes of the radiative, $\tau_r$, and non-radiative (at 0 K), $\tau_{nr}(0)$, lifetimes is an important factor. In $CsCaBr_3$:$Tm^{2+}$ $\tau_r = 1.73$ $\mu s$ and $\tau_{nr}(0) = 41$ $\mu s$. This indicates that at low temperatures, the radiative lifetime is shorter than the non-radiative lifetime, meaning that radiative emission dominates. This can be seen in figure 6.4, with the fitted parameter $\tau_r = 1.73$ $\mu s$ matching the lifetime seen at low temperatures. As the temperature rises the non-radiative lifetime shortens, and at some point becomes shorter than the radiative lifetime, the non-radiative relaxation then begins to dominate and radiative emission is quenched. In $RbCaI_3$:$Tm^{2+}$ the situation is very different, $\tau_r = 3.80$ $\mu s$ and $\tau_{nr}(0) = 0.42$ $\mu s$. Here, even at very low temperatures the non-radiative lifetime is shorter than the radiative lifetime, indicating that the emission is already somewhat

quenched at this temperature. This is indicated in figure 6.5, where the lifetime seen at low temperatures is much shorter than the fitted parameter $\tau_r = 3.80\ \mu s$. The observed lifetime is much closer to the non-radiative lifetime at this temperature, $\tau_{nr}(0) = 0.42\ \mu s$. This supports the idea that the observed lifetime is limited by the non-radiative lifetime already at very low temperatures. This also explains why no low temperature plateau of lifetimes is observed, as the quenching process has already begun.

## 6.2 Internal Conversion via Configurational Crossing

The next model to be implemented is the barrier model described in section 2.2.2. This model describes an electron in an electronic state as being in a potential well, with a potential barrier which must be overcome with phonons before non-radiative emission can occur from a state. This model is applied to analysis of the IR emission, from the $(^3\mathrm{H}_6,\mathrm{t}_{2g})S{=}3/2$ to the $^2\mathrm{F}_{7/2}$ state as seen in figure 6.6.

Here competition between the phonon assisted barrier hopping and the radiative emission is explored to give an expression for experimental lifetime as a function of temperature. This relationship is shown in equation 6.4. Here $\tau_{nr}(T)$ is the non-radiative lifetime as a function of temperature, $W_0$ is the rate of non-radiative depopulation of the zero-phonon level of the emitting state (and can be considered the probability of tunneling through the potential barrier,) $W_1$ is the rate of phonon assisted barrier hopping, $E_{nr}$ is the barrier height, $k_B$ is Boltzmanns constant, and $T$ is the temperature in Kelvin.

$$\tau_{nr}(T) = \frac{1}{W_0 + W_1 \exp\left[\frac{-E_{nr}}{k_B T}\right]} \tag{6.4}$$

As with the fitting of the multiphonon model, equation 6.4 was fit to the lifetime data as a function of temperature using a least squares fitting regime. The parameters allowed to vary were $W_0$, $W_1$, and $E_{nr}$ and the fitted values of these for the IR emission from $CsCaCl_3$:$Tm^{2+}$ and $CsCaBr_3$:$Tm^{2+}$ are listed in table 6.2 along with $\tau_0 = 1/W_0$ and $\tau_1 = 1/W_1$ which are lifetimes corresponding to the rates $W_0$ and $W_1$. The fitted model is compared to experimental data in figure 6.7 for $CsCaCl_3$:$Tm^{2+}$ and figure 6.8 for $CsCaBr_3$:$Tm^{2+}$.

In the case of $CsCaCl_3$:$Tm^{2+}$, in figure 6.7, a very good fit to the experimental data is achieved, with the model and experiment agreeing within uncertainties at all values except a couple of data points at 150 K and 170 K. The lifetime can be seen to have a gradual decline from 0 K to 50 K centering on 250 $\mu s$, then a sharp decline beginning at 50 K with the emission quenched by 150 K. In the case of $CsCaBr_3$:$Tm^{2+}$ a good fit is

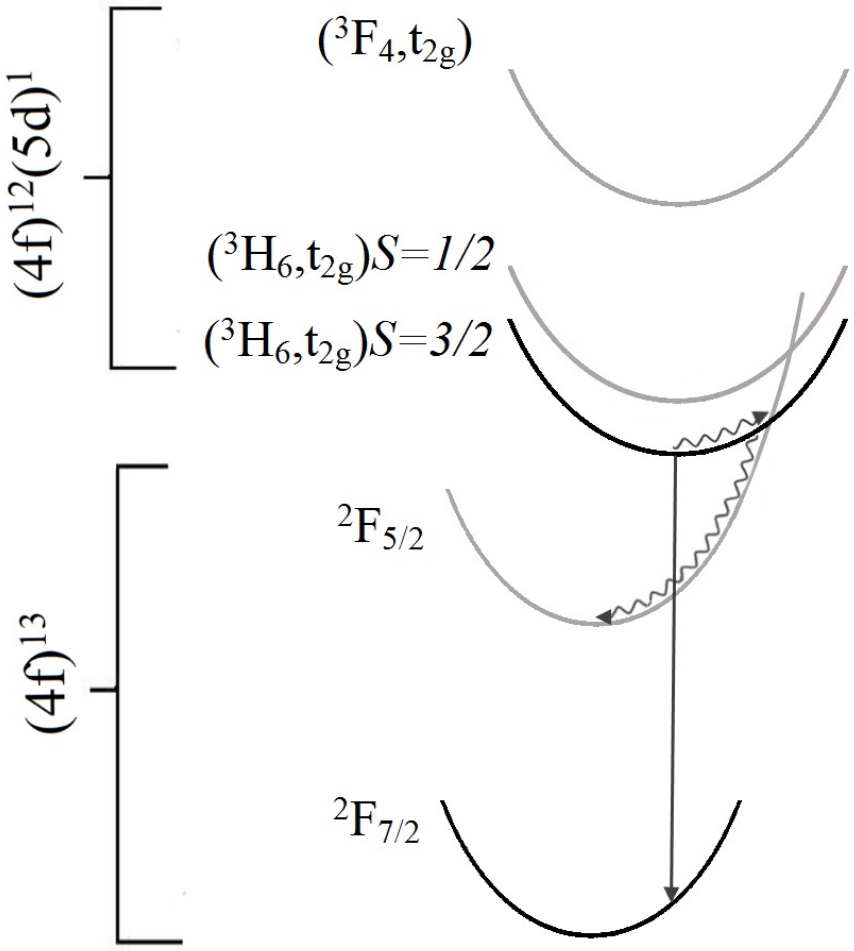


**Figure 6.6** A configurational coordinate diagram of the energy levels within the $Tm^{2+}$ ion. Energy levels within both the $(4f)^{13}$ and $(4f)^{12}(5d)^1$ configurations are shown. The radiative emission being monitored here is shown with a straight arrow between bold levels. The competing phonon assisted barrier hopping process is indicated with the curly arrows.

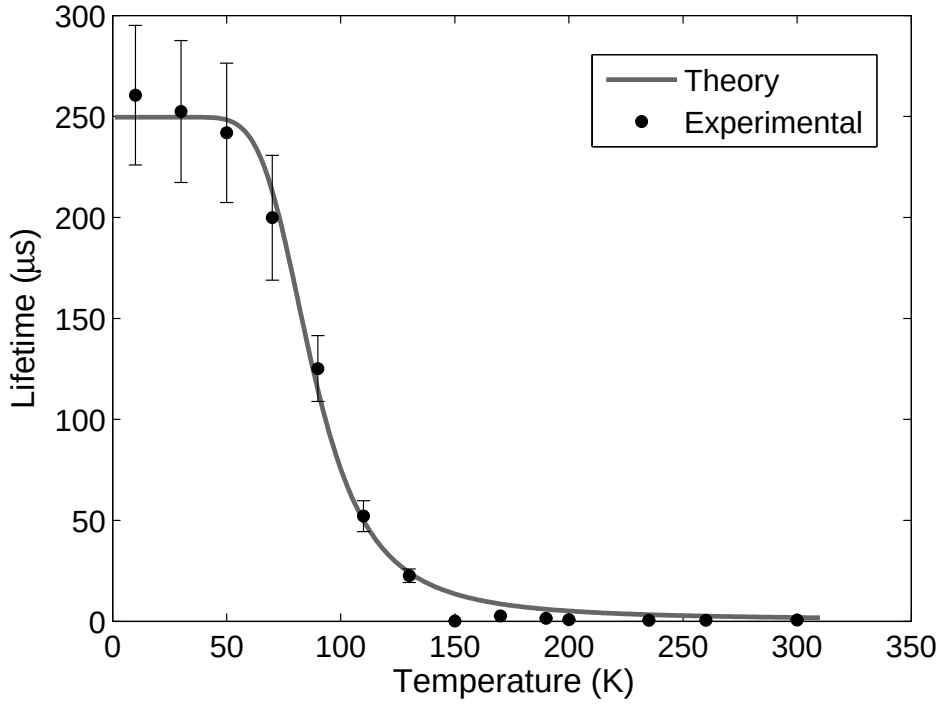


**Figure 6.7** Barrier model fitted to lifetime data for $CsCaCl_3:Tm^{2+}$. IR emission band at 12,000 $cm^{-1}$ (833 nm) being monitored. Sample excited at 28,940 $cm^{-1}$ (345 nm.)

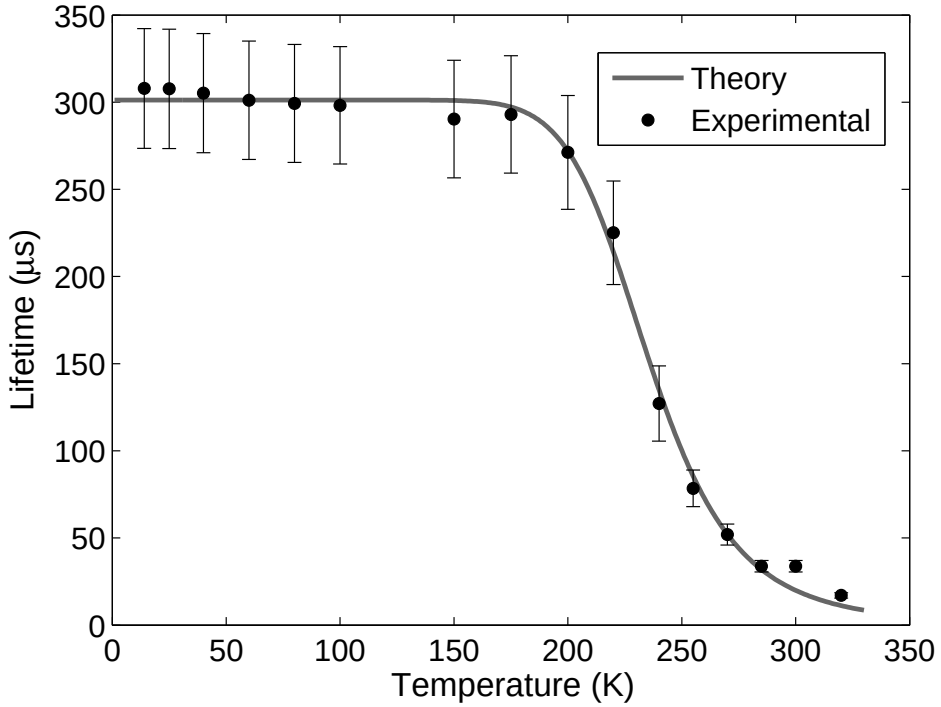


**Figure 6.8** Barrier model fitted to lifetime data for $CsCaBr_3:Tm^{2+}$. IR emission band at 12,270 $cm^{-1}$ (815 nm) being monitored. Sample excited at 28,940 $cm^{-1}$ (345 nm.)

| **Parameter** | **$CsCaCl_3:Tm^{2+}$ (Infrared Emission)** | **$CsCaBr_3:Tm^{2+}$ (Infrared Emission)** |
|---|---|---|
| $W_0$ ($s^{-1}$) | $4.01\times10^3$ | $3.32\times10^3$ |
| $\tau_0$ (s) | $2.50\times10^{-4}$ | $3.01\times10^{-4}$ |
| $W_1$ ($s^{-1}$) | $3.93\times10^6$ | $8.05\times10^8$ |
| $\tau_1$ (s) | $2.54\times10^{-7}$ | $1.24\times10^{-9}$ |
| $E_{nr}$ ($cm^{-1}$) | 420 | 2033 |

**Table 6.2** Fitted values of parameters in the barrier model described by equation 6.4 for IR emission from $CsCaCl_3:Tm^{2+}$ and $CsCaBr_3:Tm^{2+}$.

also acheived, again with the model and experimental vaules agreeing within uncertainties at all but two data points, this time at 300 K and 325 K. Here the lifetime is seen to be fairly steady at around 300 $\mu s$, up until a much higher temperature of 175 K. After 175 K a sharp decline in lifetime begins and emission is completely quenched by 325 K.

The relative sizes of the rates $W_0$ and $W_1$, or the lifetimes $\tau_0$ and $\tau_1$ is an interesting factor to consider. In section 2.2.2, when equation 6.4 was developed $W_0$ was defined to be the sum of the rate of non-radiative relaxation arising from tunneling through the barrier and of radiative relaxation. As the rate of radiative emission is much greater than the rate of tunneling, it can be thought of as the rate of radiative emission, and the lifetime $\tau_0$ can be thought of as the lifetime of radiative emission. The rate $W_1$ is the rate of phonon assisted barrier hopping, or of non-radiatve relaxation, and $\tau_1$ can be thought of as the non-radiative lifetime at 0 K. In $CsCaCl_3:Tm^{2+}$ $\tau_0 = 250\ \mu s$ and $\tau_1 = 0.254\ \mu s$. In figure 6.7 the low temperature lifetime measured agrees with the radiative lifetime calculated, so the non-radiative emission does not seem to be quenching the radiative emission at low temperatures despite having a much shorter lifetime. This is because at low temperatures there is not yet sufficiently high phonon energy in the lattice to overcome the potential barrier. At 50 K the phonon energy reaches a critical point and the potential barrier is able to be overcome, causing the longer lifetime radiative emission to be rapidly quenched. In $CsCaBr_3:Tm^{2+}$ $\tau_0 = 301\ \mu s$ and $\tau_1 = 0.00124\ \mu s$. The behaviour here is similar to $CsCaCl_3:Tm^{2+}$, although in this case the potential barrier is overcome at a higher temperature, around 175 K.

The other parameter to be considered is $E_{nr}$, the potential barrier height. In $CsCaCl_3:Tm^{2+}$

this is $E_{nr} = 420$ cm$^{-1}$ and in CsCaBr$_3$:Tm$^{2+}$ $E_{nr} = 2033$ cm$^{-1}$. The barrier height is much bigger in the case of CsCaBr$_3$:Tm$^{2+}$. This explains why the radiative emission persists to a much higher temperature. More thermal energy is required to overcome the bigger potential barrier in this case.

Applying the phonon assisted barrier hopping model to the temperature dependence of lifetime of IR emission of CsCaCl$_3$:Tm$^{2+}$ and CsCaBr$_3$:Tm$^{2+}$ has allowed physical information to be determined. Both materials have shorter lifetimes for non-radiative than radiative emission, but with the radiative emission persisting at low temperatures because a critical phonon energy must be present in the lattice to overcome the potential barriers. CsCaBr$_3$:Tm$^{2+}$ has a much larger potential barrier than CsCaCl$_3$:Tm$^{2+}$, which allows the radiative emission to persist to much higher temperatures in the former than the latter, as more thermal vibrational energy is needed to overcome the barrier.

## 6.3 Comparison of Calculated and Experimentally Determined Lifetimes

Theoretical lifetimes for the emissions being examined can be output from the calculation performed in chapter 5. This is achieved by considering the calculated Einstein A coefficients of the visible and IR transitions in these materials.

The Einstein A coefficient is a coefficient of spontaneous emission, with units $s^{-1}$. If a pair of energy levels are considered, $E_1$ and $E_2$ in figure 6.9, the $A_{21}$ coefficient is the probability per unit time that an electron in state $E_2$ will spontaneously emit a photon $hv$ and undergo a transition to energy state $E_1$.

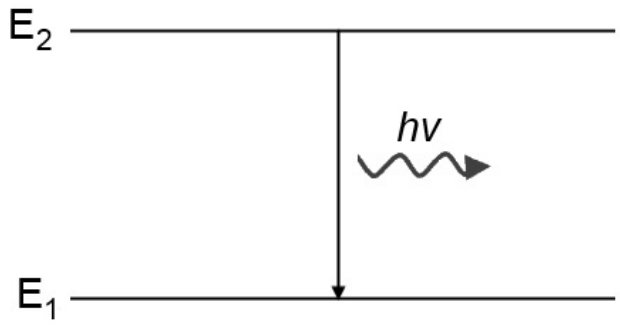


**Figure 6.9** Energy levels $E_2$ and $E_1$. The Einstein $A_{21}$ coefficient is the probability per unit time that an electron in state $E_2$ will spontaneously emit a photon $hv$ and undergo a transition to energy state $E_1$

When expressed mathematically, if there are $n_2$ particles per unit volume in state $E_2$, then the rate of change of the number density is given by equation 6.5.

$$\frac{dn_2}{dt} = -A_{21}n_2 \tag{6.5}$$

In order to obtain lifetimes from these, the Einstein A coefficients for spontaneous emission between all states involved in the given emission are added together, the lifetime for

that emission is then simply the inverse of the sum of the Einstein A coefficients.

These lifetimes were calculated for both visible and IR emission for each of the materials for which the calculation was run, and the resulting lifetimes are displayed in table 6.3 along with the experimentally determined lifetimes.

| | **$CsCaCl_3$:$Tm^{2+}$** | | **$CsCaBr_3$:$Tm^{2+}$** | | **$CsCaI_3$:$Tm^{2+}$** | |
|---|---|---|---|---|---|---|
| | **Theory** | **Experiment** | **Theory** | **Experiment** | **Theory** | **Experiment** |
| $\tau_{Vis}$ ($\mu s$) | 0.8999 | - | 0.8766 | 1.73 | 0.4783 | - |
| $\tau_{IR}$ ($\mu s$) | 628.6 | 250 | 569.3 | 301 | 709.7 | - |

**Table 6.3** Calculated and experimentally determined lifetimes for emissions from $CsCaCl_3$:$Tm^{2+}$, $CsCaBr_3$:$Tm^{2+}$, and $CsCaI_3$:$Tm^{2+}$.

Not all the lifetimes calculated were able to be experimentally measured, but those that were agree with the calculations within a factor of two or three of the lifetime. This is a good indication that both the energy level calculation and the experimentally determined lifetimes are reasonable.

## Chapter 7

# Conclusion

Divalent thulium is one of the lesser researched lanthanide ions. In this thesis it has been studied doped into a series of $AMX_3$ salts: $CsCaI_3$, $CsCaBr_3$, $CsCaCl_3$ and $RbCaI_3$.

The energy structure of the $Tm^{2+}$ ion was examined by performing parameterised energy level calculations for $CsCaI_3$, $CsCaBr_3$ and $CsCaCl_3$. Optimisation of the parameters was achieved by comparing simulated spectra generated by the calculation to experimental spectra. The calculated energy levels, optimised crystal field parameters and simulated optical absorption spectra are presented. Theoretical predictions yield excellent approximation to the experimental data.

The decay profile of emission from $CsCaCl_3$, $CsCaBr_3$, and $RbCaI_3$ has been measured using a pulsed dye laser for the ($^3F_4$,$t_{2g}$) and ($^3H_6$,$t_{2g}$) excited (emitting) states. The temperature dependence of this decay from 10 K up to room temperature was recorded. Two methods of modeling this relationship have been examined.

First a multiphonon model, considering the competition between radiative emission and a cascade of phonons as depopulation methods from a state is considered. Visible emission from the ($^3F_4$,$t_{2g}$) state is modelled in this way, and multiphonon relaxation to the ($^3H_6$,$t_{2g}$) levels is considered. This model is used for $CsCaBr_3$ and $RbCaI_3$ doped with $Tm^{2+}$, as these were the materials from which this visible emission could be observed. The 10 K and 28 K lifetimes yielded are 1.7 $\mu s$ and 0.40 $\mu s$ for $CsCaBr_3$ and $RbCaI_3$ respectively. In both cases no emission is observed at room temperature. This model provides a good fit to the data, and effective phonon energies in the range 100-200 $cm^{-1}$ are output, which is consistent with the phonon density of states in these low phonon energy hosts.

Secondly a model considering phonon assisted barrier hopping and radiative emission as competing depopulation methods is considered. Infrared emission from the ($^3H_6$,$t_{2g}$) states is modelled this way. This model is used for $CsCaBr_3$ and $CsCaCl_3$ doped with $Tm^{2+}$, as these were the materials from which this infrared emission could be observed. The14 K and 10 K lifetimes yielded are 301 $\mu s$ and 250 $\mu s$ for $CsCaBr_3$ and $CsCaCl_3$ respectively. For $CsCaBr_3$ this value reduces to 270 $\mu s$ at 200 K and is not quenched until 300 K, whilst for $CsCaCl_3$ emission is comletely quenched by 170 K. This temperature dependent behavior is interpreted in terms of internal conversion via configurational crossing between the excited and ground state potential energy surfaces. The potential barrier for non-radiative relaxation is found to be five times larger in $CsCaBr_3$ compared to $CsCaCl_3$. This explains the fact that emission is still observable in the bromide host at room temperature.

Theoretical radiative lifetimes were determined from the energy level calculations, and compared to those output by the multiphonon and barrier models. Lifetimes from each of these methods were found to agree within an order of magnitude of the lifetime. This is a good indication that both the energy level calculation and the experimentally determined lifetimes are reasonable.

# Acknowledgements

I have been fortunate enough to have the support and advice of many very clever people throughout the process of completing this thesis. Thank you to my supervisors Mike Reid and Jon-Paul Wells who have provided me with invaluable guidance through the entire procedure. The help of Konstantin Ivanovskikh and Alex Neiman in completing experimental work was crucial and much appreciated. The advice of Roger Reeves and his ability to make lab equipment seemingly magically work was also invaluable. The constant willingness to help of Pubudu Senanayake, Rosa Hughes-Currie and Alex Salkeld is also gratefully acknowledged. Finally thanks to Emil, for his support and for enduring me throughout the entire process.

# References


[1] J. Grimm and H.U. Güdel. Five different types of spontaneous emission simultaneously observed in $Tm^{2+}$ doped $CsCaBr_3$. *Chemical Physics Letters*, 404(1-3):40–43, 2005.

[2] E. Beurer, J. Grimm, P. Gerner, and H.U. Güdel. New type of near-infrared to visible photon upconversion in $Tm^{2+}$-doped $CsCaI_3$. *Journal of the American Chemical Society*, 128(10):3110–3111, 2006.

[3] B.G. Wybourne. *Spectroscopic Properties of Rare Earths*. John Wiley & Sons Inc., New York, 1965.

[4] J. Grimm, E. Beurer, and H.U. Güdel. Crystal absorption spectra in the region of 4f-4f and 4f-5d excitations in $Tm^{2+}$-doped $CsCaCl_3$, $CsCaBr_3$, and $CsCaI_3$. *Inorganic Chemistry*, 45(26):10905–10908, 2006.

[5] J. Grimm, E. Beurer, P. Gerner, and H.U. Güdel. Upconversion between 4f-5d excited states in $Tm^{2+}$-doped $CsCaCl_3$, $CsCaBr_3$, and $CsCaI_3$. *Chemistry-A European Journal*, 13(4):1152–1157, 2007.

[6] G.W. Burdick and M.F. Reid. *Handbook on the Physics and Chemistry of Rare Earths*, volume 37. Elsevier, 2007.

[7] G.H. Dieke. *Spectra and Energy Levels of Rare Earth Ions in Crystals*. Interscience Publishers, 1968.

[8] W.T. Carnall, G.L. Goodman, K. Rajnak, and R.S. Rana. Luminescence and photoionisation processes of $Yb^{2+}$ in $CaF_2$, $SrF_2$ and $BaF_2$. *J. Chem. Phys.*, page 3443, 1989.

[9] R. Chang. *Chemistry*. McGraw-Hill Higher Education, ninth edition, 2007.

[10] R. Powell. *Physics of Solid-State Laser Materials*. Springer-Verlag New York, Inc., New York, 1998.

[11] B. Henderson and G.F. Imbusch. *Optical Spectroscopy of Inorganic Solids*. Oxford University Press, New York, 1989.

[12] B. Henderson and R.H. Bartram. *Crystal-Field Engineering of Solid State Laser Materials*. Cambridge University Press, New York, 2000.

[13] K.V. Ivanovskikh, M.F. Reid, and A. Meijerink. Spectroscopy and relaxation dynamics of high-energy $4f^{11}5d$ states of $Tm^{3+}$ ions doped into $CaF_2$. *Manuscript in Preparation - Private Communication*.

[14] L.A. Riseberg and H.W. Moos. Multiphonon Orbit-Lattice Relaxation of Excited States of Rare-Earth Ions in Crystals. *Phys. Rev.*, 174:429–438, Oct 1968.

[15] J.R. Wells, M Grinberg, K Wynne, and T.P.J Han. Femtosecond pump-probe measurements of non-radiative relaxation in $LiAlO_2:V^{3+}$. *Journal of Physics: Condensed Matter*, 18(16):3967, 2006.

[16] N.F. Mott. On the Absorption of Light by Crystals. *Proceedings of the Royal Society of London. Series A. Mathematical and Physical Sciences*, 167(930):384–391, 1938.

[17] E. Beurer, J. Grimm, P. Gerner, and H.U. Güdel. Absorption, Light Emission, and Upconversion Properties of $Tm^{2+}$-Doped $CsCaI_3$ and $RbCaI_3$. *Inorganic Chemistry*, 45(24):9901–9906, 2006.

[18] E. Beurer. Synthesis and Optical Light Absorption and Emission Properties of $Tm^{2+}$ Doped into $CsCaI_3$ and $RbCaI_3$ Crystals. Diploma thesis, University of Bern.

[19] J. Grimm, E. Beurer, and H.U. Güdel. Crystal Absorption Spectra in the Region of 4f-4f and 4f-5d Excitations in $Tm^{2+}$-Doped $CsCaCl_3$, $CsCaBr_3$, and $CsCaI_3$. *Inorganic Chemistry*, 45(26):10905–10908, 2006. PMID: 17173449.

[20] G. Sánchez-Sanz, L. Seijo, and Z. Barandiarán. Energy Gaps in the $4f^{13}5d^1$ Manifold and Multiple Spontaneous Emissions in $Yb^{2+}$-Doped $CsCaBr_3$. *The Journal of Physical Chemistry A*, 113(45):12591–12598, 2009. PMID: 19658413.

[21] J. Grimm, O.S. Wenger, K.W. Krämer, and H.U Güdel. 4f-4f and 4f-5d excited states and luminescence properties of $Tm^{2+}$- doped $CaF_2$, $CaCl_2$, $SrCl_2$ and $BaCl_2$ . *Journal of Luminescence*, 126(2):590 – 596, 2007.

[22] F. Auzel. Upconversion and Anti-Stokes Processes with f and d Ions in Solids. *Chemical Reviews*, 104(1):139–174, 2004. PMID: 14719973.

[23] R. Hughes-Currie, M.F. Reid, J. Grimm, and H.U. Güdel. Crystal field and vibrational analysis of the spectrum of $SrCl_2:Tm^{2+}$. *Manuscript in Preparation - Private Communication*.

[24] G. Sánchez-Sanz, L. Seijo, and Z. Barandiarán. $Yb^{2+}$-doped $SrCl_2$: Electronic structure of impurity states and impurity-trapped excitons. *The Journal of Chemical Physics*, 133(11):114509, 2010.

[25] A.J. Salkeld, M.F. Reid, J.R. Wells, G. Sánchez-Sanz, L. Seijo, and Z. Barandiarán. Effective Hamiltonian parameters for ab initio energy-level calculations of $SrCl_2$:$Yb^{2+}$ and $CsCaBr_3$:$Yb^{2+}$. *Journal of Physics: Condensed Matter*, 25(41):415504, 2013.